buffered saline (pH 7.5) at room temperature for 30 min and incubated with a monoclonal antibody against LC3 (anti-LC3, 1:40000; Medical & Biological Laboratories, Co., Nagoya, Japan) or dynactin 1 (anti-dynactin 1 H300; 1:2000; Santa Cruz, Santa Cruz, CA, USA) overnight at 4°C. The subsequent procedures were carried out using the EnVision+Kit/HRP (DAB) (DAKO, Glostrup, Denmark) according to the manufacturer's protocol.

Quantitative assessment of immunohistochemistry. To assess LC3 immunoreactivity in spinal motor neurons, we included 4 ALS patients and 4 disease controls, and prepared 5 independent specimens from each subject. We counted about 200 motor neurons in ALS patients and about 400 neurons in control patients. The intensity of immunohistochemistry signals was quantified using a BZ-8000 fluorescent microscope and its software (BZ-Analyzer; Keyence, Osaka, Japan). Signal intensity was expressed as the individual intracellular cytoplasmic signal level (arbitrary absorbance units/mm^2) per motor neuron by subtracting the mean background levels of 3 regions of interest in each section. The ventral spinal horn was defined as the gray matter ventral to the line through the central spinal canal perpendicular to the ventral spinal sulcus. To investigate the correlation between dynactin 1 and LC3 in individual motor neurons we used consecutive transverse spinal cord sections.

***In situ* hybridization.** *In situ* hybridization for human tissue was performed as described previously [13]. We provide the detailed information in Materials and Methods S1.

Electron microscopy. Electron microscopy was performed on samples from 2 sporadic ALS patients (71 years-old male and 62 years-old female) and 2 disease control patients (68 years old male with multiple system atrophy and 60 years-old male with multiple system atrophy). Epoxy resin-embedded specimens of spinal anterior horn were cut into 70-nm ultrathin sections. Ultrathin sections were contrasted by staining with uranyl acetate and lead citrate. Sections were viewed with a JEM-1400EX electron microscope (JEOL, Tokyo, Japan) at 80 kV.

Protocols for *C. elegans*

Ethics statement. All animal experiments were performed in accordance with the National Institute of Health Guide for the Care and Use of Laboratory Animals and were approved by the Nagoya University Animal Experiment Committee.

Culture of *C. elegans*. Standard methods were used to culture *C. elegans* on nematode growth medium (NGM) agar [18]. The animals were maintained at 20°C unless otherwise indicated. We provide the detailed information in Materials and Methods S1.

Constructs and *C. elegans* Strains. To generate transgenic *C. elegans*, plasmid DNA encoding acr2promotor::*shRNA*::*gfp* was injected into the gonads of young adult hermaphrodite N2 worms. We provide the detailed information for the shRNA vector and other co-injected proteins, i.e., SNB-1 and Lgg1, in Materials and Methods S1.

Whole Mount *in situ* Hybridization. Whole mount *in situ* hybridization of worms was performed as described previously [13,19]. We provide the detailed information in Materials and Methods S1.

Phenotypic analysis of *C. elegans*. A lifespan assay was performed as described preciously [20], with some modifications. The Worms were allowed to lay eggs on a dish for 3–6 h to obtain synchronous progeny for the experiment. L4 worms were collected and transferred every 3 days to a fresh plate until the end of their reproductive life. The animals were scored as dead if they did not move when prodded with a platinum pick and did not show pharyngeal pumping.

A body bend assay, liquid thrashing assay, and video capture analysis were performed as locomotion assays. To examine the body bend frequency, exposed worms were transferred onto a fresh NGM plate and scored for the number of body bends

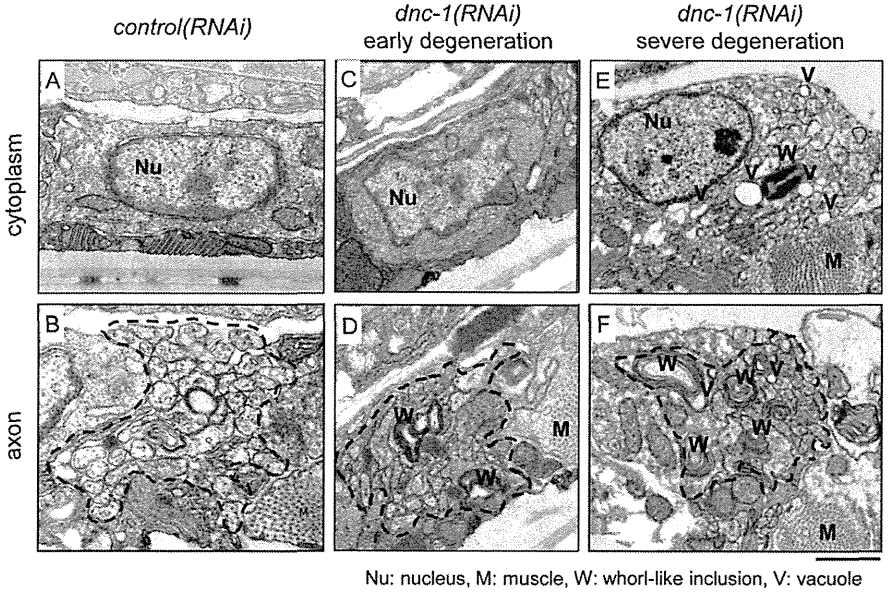

Figure 5. Ultrastructure of degenerating motor neurons. Electron microscopy of transverse sections of ventral motor neurons from the *control(RNAi)* (*A, B*) and *dnc-1(RNAi)* (*C–F*) worms. The dashed lines in *B*, *D*, and *F* denote the boundaries of the main bundle of axons. Each round-shaped component inside the dashed line is an axon. In the *dnc-1(RNAi)* worms, whorl-like inclusions (W) and vacuoles (V) were observed (*D–F*). In the worms with mild axonal degeneration (*D*), few morphological changes were observed in the cytoplasm (*C*); however, in the later stage with severe axonal degeneration (*F*), the cell bodies were also affected (*E*). Scale bars = 20 μm.
doi:10.1371/journal.pone.0054511.g005

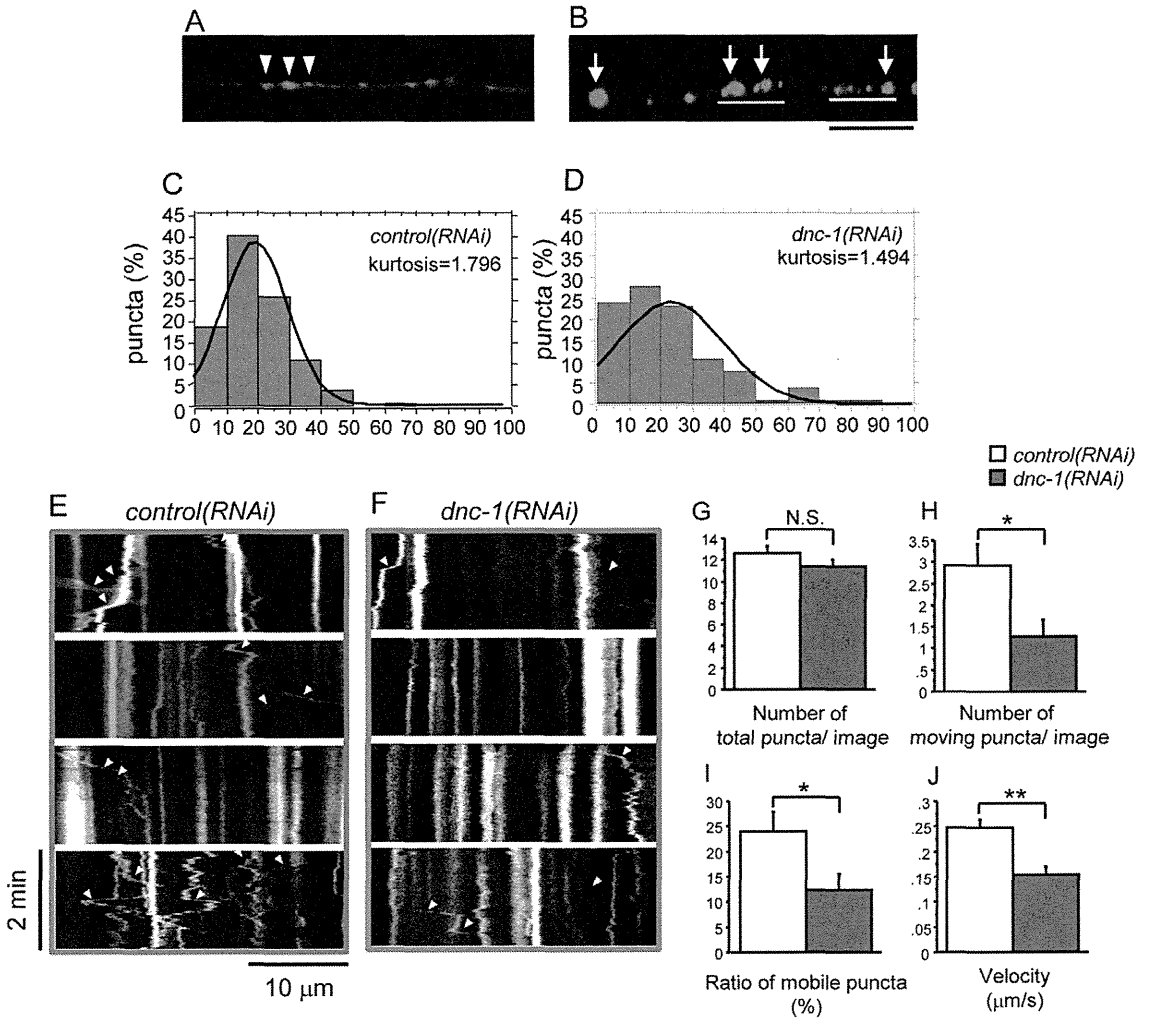

Figure 6. Defective axonal transport of synaptobrevin-1 in *dnc-1(RNAi) C. elegans*. (*A, B*) Expression patterns of DsRed-tagged synaptobrevin-1 (SNB-1) in the dorsal nerve cord. In the *control(RNAi)* worms, SNB-1 puncta (arrowheads) are regularly spaced with a uniform shape. In the *dnc-1(RNAi)* worms (B), they are irregularly spaced and abnormally accumulated (white bars) with occasional clumps. (*C, D*) Histograms of the distances between neighboring SNB-1 puncta. The average distance between puncta in the *control(RNAi)* (3.240±1.716 μm, n = 139) and *dnc-1(RNAi)* (3.855±2.764 μm, n = 104) worms was not significantly different (p = 0.996 by Student's t test), but the peak of the control histogram was higher than that of the *dnc-1(RNAi)* histogram, proving that the localization of SNB1 was irregular. (*E, F*) Representative kymographs of SNB-1::DsRed in the ventral nerve cord from the *control(RNAi)* (*E*) and *dnc-1(RNAi)* (*F*) worms derived from time-lapse imaging. Vertical lines represent stationary/docked SNB-1 puncta and oblique lines (labeled with yellow arrowheads) represent the tracks of moving SNB-1 puncta. The slope of this track is an indicator of velocity. (*G*) The number of SNB-1 puncta within a single image of kymograph was not different between the *control(RNAi)* and the *dnc-1(RNAi)* worms. (*H*) The mean velocities of SNB-1 puncta. (*I, J*) The quantitative analysis of mobile puncta. The number of puncta which moved more than 2 μm was counted (*I*). The ratio of moving puncta was calculated by dividing the number of moving puncta by the total number of SNB-1 puncta (*J*). A total of 20 time laps images were analyzed from each strains in *G–J*. Scale bar (black) = 10 μm (*B*). Statistical analyses were performed using Student's t test (*p<0.05, **p<0.001, ***p<0.0001). Error bars are S.E.M.
doi:10.1371/journal.pone.0054511.g006

performed in 3 min. A body bend was defined as a change in the direction of the part of the worm corresponding to the posterior bulb of the pharynx along the y-axis, assuming that the worm was traveling along the x-axis. We also performed a liquid thrashing assay as described previously [21], with some modifications. Briefly, the worms were put on a 6-cm NGM-coated plate with 3 ml of M9 media. The worms were allowed to settle for 30 s, their movements were captured by video for 30 s, and the number of thrashing movements was counted. We also analyzed the speed of movement using a video capture system as described previously [22]. Briefly, fully matured, adult worms were transferred individually to agar plates with no food. The movement of each worm was observed for 5 min and recorded using video equipment (Olympus, Tokyo, Japan) with a sampling rate of 30 frames/s. A computer-controlled microscope stage was automatically moved to center the worms in the visual field using a custom image analysis algorithm within the microscope's software package (MetaMorph; Universal Imaging Corp., West Chester, PA, USA). The midlines of the recorded worms were extracted from each image. All strains were randomized and scored on the same day.

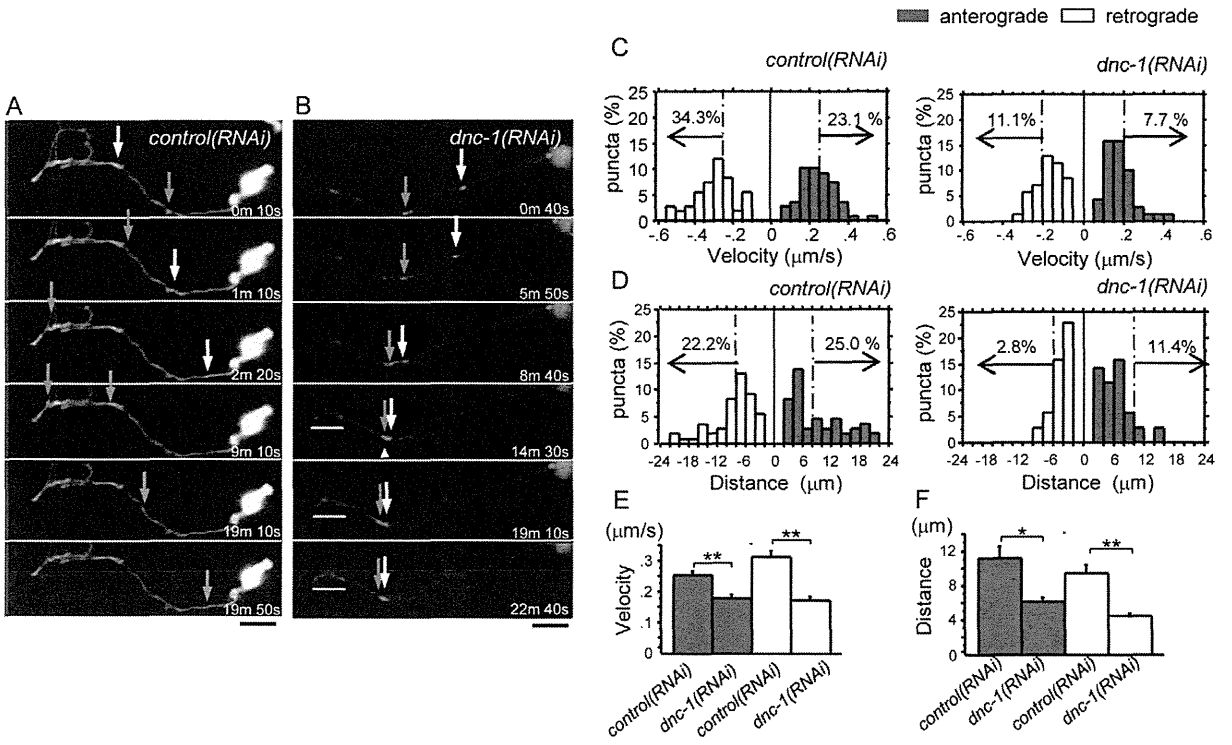

Figure 7. Impaired transport and abnormal accumulation of autophagosomes in the axons of *dnc-1(RNAi)* motor neurons. (*A, B*) Representative time-lapse images of autophagosome (DsRed-tagged Lgg1) transport in an axon (GFP-tagged shRNA; green) of a primary cultured motor neuron from the *control(RNAi)* (*A*) and *dnc-1(RNAi)* (*B*) worms. The autophagosomes were transported smoothly along the axon (arrows) of the *control(RNAi)* motor neuron (*A*). The autophagosome (arrows) was transported anterogradely, but was trapped where the axon was slightly narrowed (arrowhead) (*B*). There were also autophagosomes that accumulated in the distal part of the axon (*B*, bar). (*C*) Histograms of Lgg1::DsRed velocity in the retrograde (white bars) and anterograde (black bars) directions in neurons from the *control(RNAi)* and *dnc-1(RNAi)* worms. (*D*) Histograms of Lgg1::DsRed run-length in the *control(RNAi)* and *dnc-1(RNAi)* neurons. (*E, F*) Mean velocity (*E*) and run-length (*F*) of autophagosomes (n = 70 vesicles for each strain) in *control(RNAi)* and *dnc-1(RNAi)* neurons. Scale bar = 5 μm (A and B). The statistical analyses in *E* and *F* were performed using the Mann-Whitney U test (*$p<0.05$ and **$p<0.0001$). The error bars are S.E.M.
doi:10.1371/journal.pone.0054511.g007

Preparation of starved worms for the dietary restriction assay. All worms were synchronized by egg preparation [23]. The eggs were incubated at 20°C for 48 h in liquid medium. After 48 h, newly hatched worms were washed 3 times with distilled water, transferred to S basal medium without OP50, and incubated for 24 h. Worms were then picked randomly and used for the liquid thrashing assay.

Drug treatment. The worms were synchronized by egg preparation and incubated at 20°C for 24 h in liquid medium. They were then treated with rapamycin (LC Laboratories, Woburn, MA, USA) dissolved in ethanol at a final concentration of 10 or 100 μM, 3-methyladenine (3-MA) (SIGMA) dissolved in DMSO at a final concentration of 1 or 10 mM, or trichostatin A (TSA) (Tokyo Chemical Industry, Co., Tokyo, Japan) dissolved in DMSO at a final concentration of 1, 10, or 100 μM and incubated in liquid medium for 48 h. For controls (0 μM), ethanol or DMSO was added. Worms were then picked randomly and used for the liquid thrashing assay or microscopic analysis.

Primary neuronal cell cultures of nematodes. Primary neuronal cell cultures were prepared as described previously [24], with some modifications. In the present study, in order to obtain larger number of gravid animals, we cultured the worms in liquid medium (S basal medium with concentrated OP50) as described previously [25]. After incubation in liquid medium for 3 days, we performed egg isolation using lysis buffer (0.5 M NaOH/1% NaClO). Then we removed eggshell by enzymatic digestion using chitinase (SIGMA) and isolated embryonic cells were plated onto peanut lectin-coated glass bottom dishes (IWAKI, Tokyo, Japan).

Microscopic analysis. The worms were anesthetized by placing them in an 8-μl drop of levamisole (2 mM) on solidified pads of 2% agarose laid on slides. After coverslipping, the worms were examined under an LSM710 confocal microscope (Carl Zeiss Inc., Thornwood, NJ, USA). The regularity of SNB-1::DsRed localization/spacing was evaluated by measuring the distance between two neighboring fluorescent puncta of SNB-1::DsRed using ImageJ 1.43 software (National Institutes of Health). The axonal defasciculation index was measured as follows. The ventral nerve cord was divided into compartments consisting of two neighboring motor neurons. We counted the number of compartments with axonal defasciculation and divided it by the total number of compartments.

In vivo analysis of autophagosome mobility was performed as follows. Lgg1::DsRed worms were plated on an agar pad and observed using confocal microscopy. The red puncta, which represent autophagosomes, were observed for 1 min. The number of autophagosomes that moved within 1 min was divided by the total number of autophagosomes observed.

***In vitro* transport assay and image analysis.** Time-lapse images were acquired at room temperature using a 63× oil-immersion objective (N.A 1.4) for live-cultured neuron analysis at

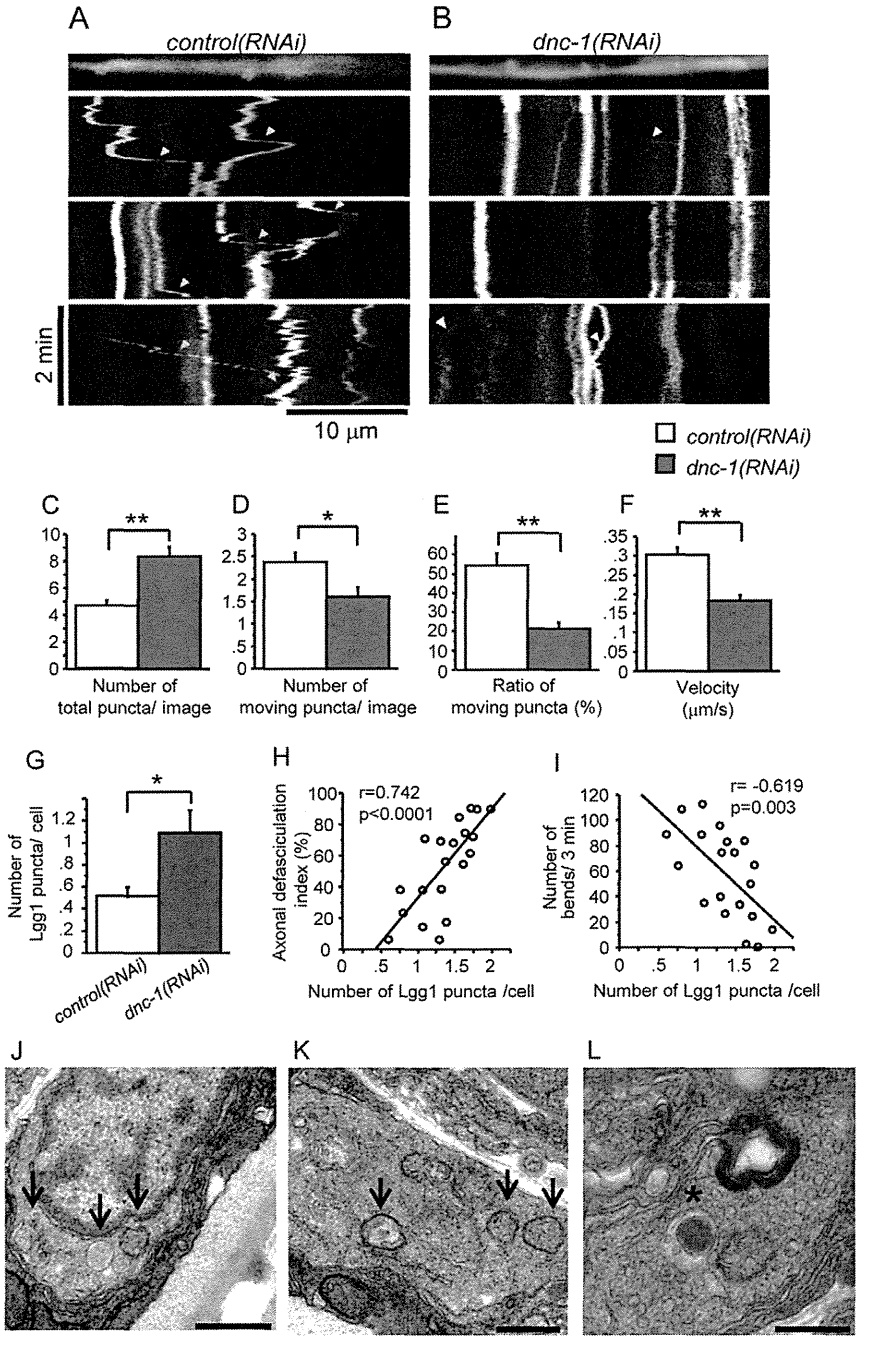

Figure 8. Accumulation of autophagosomes and motor neuron degeneration in the *dnc-1(RNAi)* worms. (*A, B*) Representative kymographs of Lgg1::DsRed in the ventral nerve cord from the *control(RNAi* (*A*) and *dnc-1(RNAi)* (*B*) worms derived from time-lapse images. Vertical lines represent stationary/docked Lgg1 puncta, while the oblique lines (labeled with arrowheads) represent the tracks of moving Lgg1 puncta. The slope of this track is an indicator of velocity. (*C*) The number of Lgg1 puncta within a single kymograph image. (*D, E*) Quantitative analyses of the mobility of puncta. The number of puncta that moved more than 2 μm was counted (*D*). The ratio of moving puncta was calculated by dividing the number of moving puncta by the total number of puncta (*E*). (*F*) The mean velocities of Lgg1 puncta. A total of 20 time-lapse images were analyzed for each strain in *C–F*. (*G*) The number of Lgg1 puncta was increased in the *dnc-1(RNAi)* worms compared with the *control(RNAi)* worms (n = 15 for each group). (*H, I*) Accumulation of autophagosomes in the *dnc-1(RNAi)* worms was correlated with the severity of axonal defasciculation (*H*) and locomotor function (*I*) (n = 20 for each analysis). (*J–L*) Ultrastructural images of ventral motor neurons from the *dnc-1(RNAi)* worms. Aberrant membranous vesicles including degenerated mitochondria were observed in the cytoplasm (*J*) and axons (*K*) (arrows). Autophagosome-like, double membrane vesicles (asterisk in *L*) were also found in the axons of the *dnc-1(RNAi)* worms (*L*). Scale bar = 500 nm (A–C) or 10 μm (D). Statistical analyses were performed using Student's t test (*$p<0.05$ and **$p<0.0001$) and Pearson's correlation coefficient in *H* and *I*. The error bars are S.E.M.
doi:10.1371/journal.pone.0054511.g008

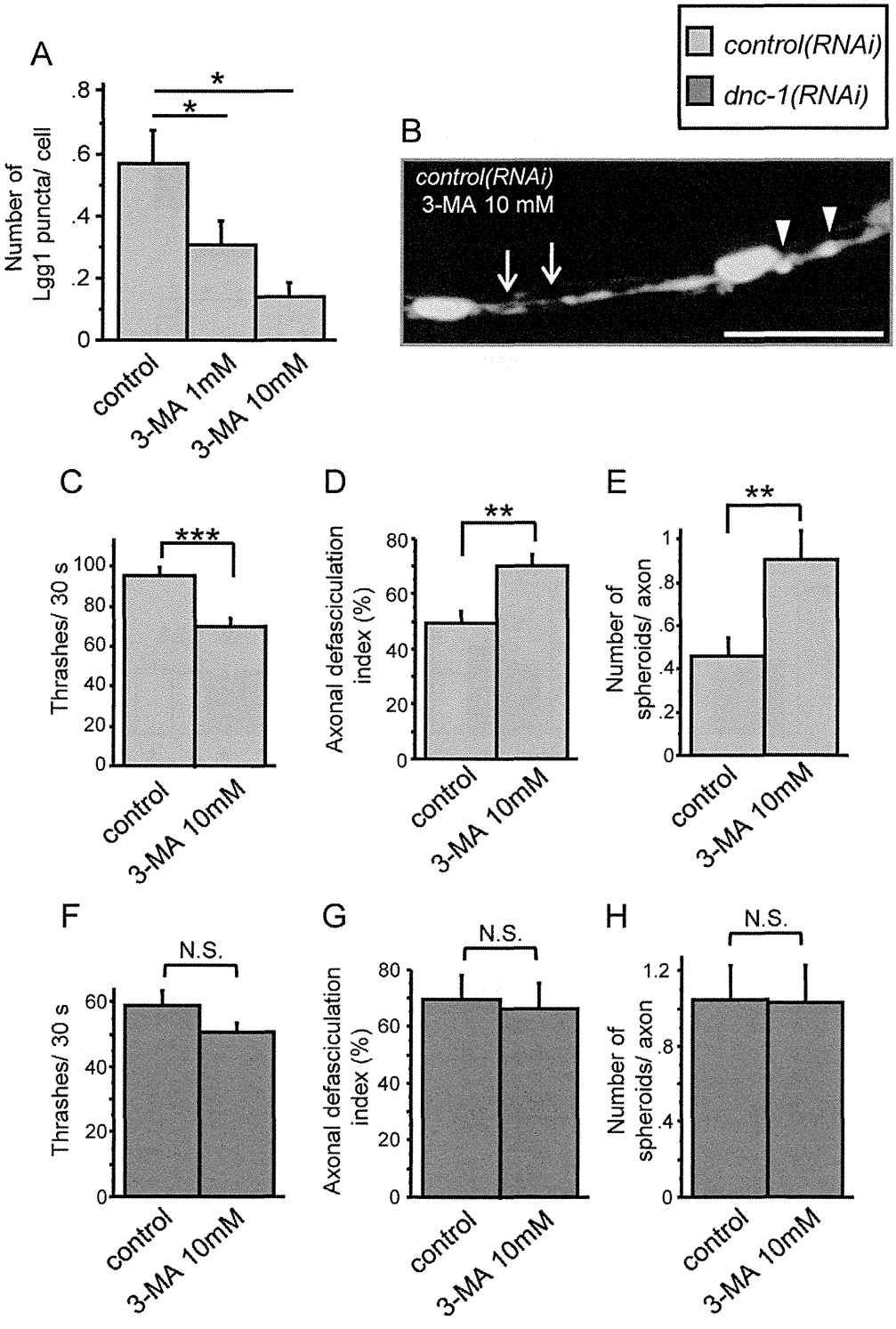

Figure 9. Dysfunction of autophagy causes axonal degeneration. (*A*) Treatment with 3-MA decreased the number of autophagosomes in the ventral nerve cord in a dose dependent manner (n = 15 for each group). (*B–E*) The effects of 3-MA on the locomotor function (*C*) and axonal morphology (*B, D,* and *E*) of the *control(RNAi)* worms. Treatment with 3-MA increased axonal defasciculation (arrows in *B* and the graph in *D*) and the number of axonal spheroids (arrowheads in *B* and the graph in *E*) (n = 15 for each group). (*F–H*) The effects of 3-MA on the locomotor function (*F*) and axonal morphology (*G, H*) of the *dnc-1(RNAi)* worms (n = 15 for each group). Scale bar = 10 μm. Statistical analyses were performed using Dunnett's post hoc test (*A*) and Student's t test (B, *D,* and *E*) (*$p<0.05$, **$p<0.001$, and ***$p<0.0001$). The error bars are S.E.M.
doi:10.1371/journal.pone.0054511.g009

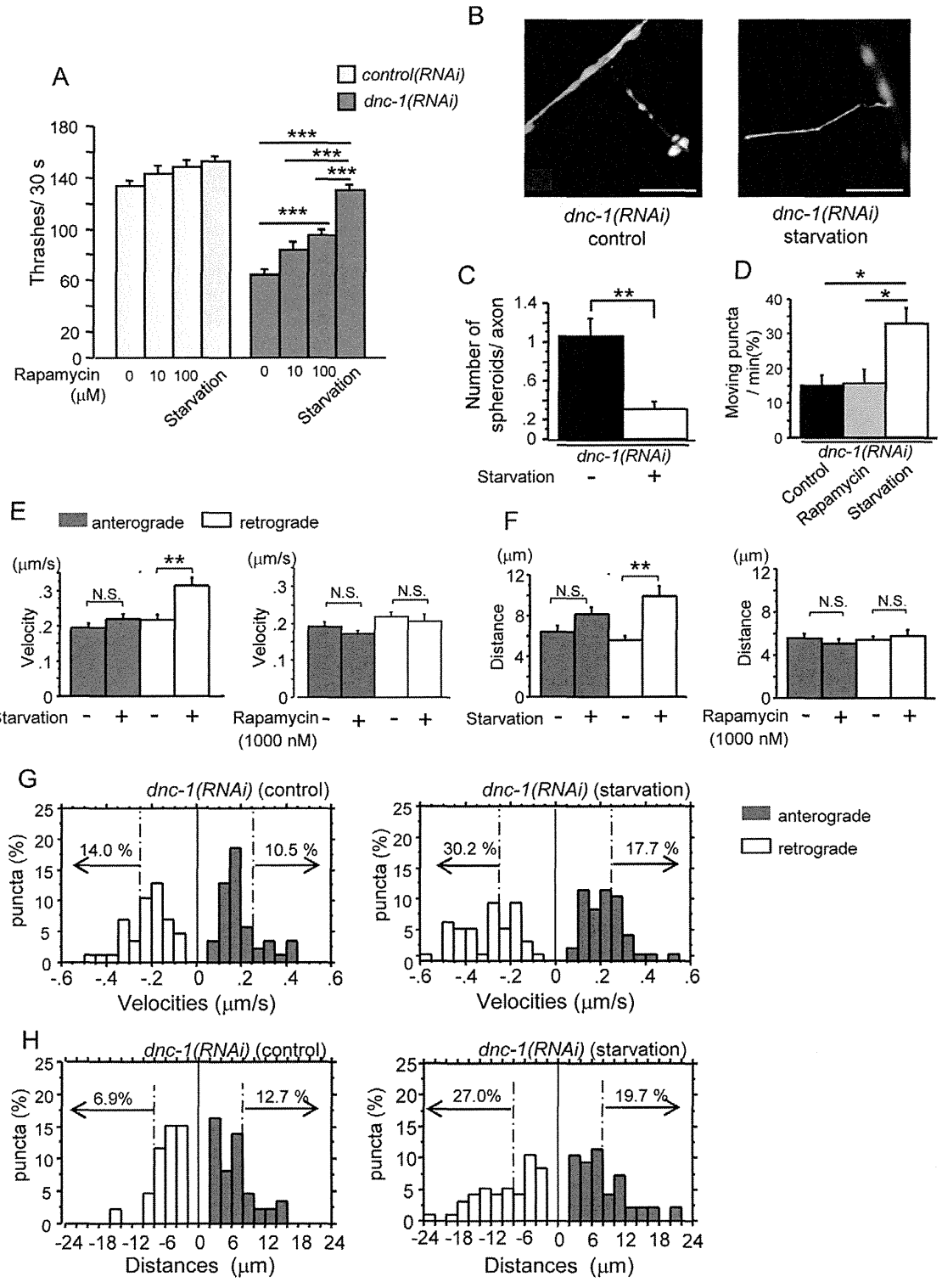

Figure 10. Starvation stimulates the retrograde transport of autophagosomes and attenuates axonal degeneration in the *dnc-1(RNAi)* worms. (*A*) Effect of rapamycin and starvation on locomotor function in the *control(RNAi)* and *dnc-1(RNAi)* worms (n = 50 for each group). (*B*) Fluorescent microscopy showing the morphological changes in axons after starvation in the *dnc-1(RNAi)* worms. (*C*) The number of axonal spheroids per transverse axon section in the *dnc-1(RNAi)* worms with or without starvation. (n = 15 animals for each treatment). (*D*) Effect of rapamycin (100 μM) and starvation on autophagosome mobility in the *dnc-1(RNAi)* worms. (n = 15 animals for each treatment). (*E, F*) Effect of rapamycin (100 μM) and starvation on the mean velocity (*E*) and run-length (*F*) of autophagosomes (black bars: anterograde transport; white bars: retrograde transport) (n = 70

vesicles for each treatment). (*G, H*) Histograms of Lgg1::DsRed velocity (*F*) and run-length (*G*) in the anterograde (black bars) and retrograde (white bars) direction in primary motor neurons from the *dnc-1(RNAi)* worms cultured with normal (control) and serum-free (starvation) medium. Scale bars = 5 μm. Statistical analyses were performed by one-way ANOVA followed by the Bonferroni/Dunn post hoc test (*A*) and Dunnett's post hoc test (*D*). Student's t test (*C*) and Mann-Whitney test (*E, F*) were used for two-group comparison (*p<0.05, **p<0.001, and ***p<0.0001). The error bars are S.E.M.

doi:10.1371/journal.pone.0054511.g010

1–2 frames/s. The images were analyzed using Zen2008 (Zeiss) software. The run-length of Lgg-1 in primary motor neurons was measured by drawing a line over moving fluorescent puncta using Zen2008. Motile puncta were counted only if they moved continuously in the same direction for more than 2 frames and if their displacement was at least 2 μm. Some runs were terminated by a pause or reversal. To ensure the accuracy of the run-length measurements, we excluded moving puncta at the beginning and end of the movie. The velocity of Lgg-1 movements was obtained from the total distance traveled divided by the duration of the run.

***In vivo* transport assay and image analysis.** Time-lapse images were acquired at room temperature using a 63× objective (N.A. 1.4) for live-worm analysis at 1 frame/s. The images were analyzed using Image J 1.43 software (National Institutes of Health). First, individual tracks of SNB-1 or Lgg1 movement were analyzed using the Multiple Kymograph plug-in, as described previously [26]. The velocity of the moving vesicles was tracked manually and their instantaneous velocity was extracted. To calculate the ratio of moving versus total vesicles, the number of vesicles that moved more than 2 μm during each time lapse period was divided with the total number of particles in each acquisition.

Electron microscopy of *C. elegans*. A conventional two-step fixation method was performed as described previously [27]. We provide the detail information in Materials and Methods S1.

Western Blot Analysis and Quantitative real-time PCR. Western blot analyses and quantitative real-time PCR were performed as described previously [28,29]. We provide a detail description in Materials and Methods S1.

Statistical analysis. Statistical analyses were performed using StatView software version 5 (Hulinks, Tokyo, Japan). We used the Kaplan-Meier and log-rank test, Student's t-test, Mann-Whitney U test, and one-way analysis of the variance (ANOVA) with the Bonferroni or Dunnett's post-hoc test. Pearson's correlation coefficient was used to assess the correlation of variables.

Results

Dysregulated dynactin 1 expression and autophagy in degenerated spinal motor neurons in SALS patients

The expression of the *DCTN1* gene was markedly reduced in the spinal motor neurons of SALS patients, as reported previously [9,13] (Fig. 1*A*). Recent studies indicate that the dysregulation of autophagy in motor neurons is a pivotal event in ALS [8,10]; thus, we investigated the relationship between decreased dynactin 1 expression and autophagy in SALS. Immunohistochemistry using consecutive sections of autopsied human spinal cords revealed that LC3 immunoreactivity, a histological marker of autophagy, was increased in the motor neurons of SALS patients in which dynactin 1 expression was decreased (Fig. 1*B*). Conversely, there was no change in the immunoreactivity for dynactin 1 and LC3 in cerebellar Purkinje cells, which showed no degeneration (Fig. 1*C*). Quantitative analysis revealed that anti-LC3 immunoreactivity was significantly increased in the spinal motor neurons of SALS patients ($p<0.0001$) (Fig. 1*D*), and was inversely correlated with the decreased mRNA levels of *DCTN1* (Fig. 1*E*) and cell size (Fig. 1*F*) in the motor neurons of SALS patients, indicating that the dysregulation of autophagy is associated with the decreased expression of dynactin 1 in SALS. Electron microscopy of sections from the SALS and control patients (Fig. 1*G, H*) also revealed that there was an abundance of autophagic vacuoles, e.g., multilamellar bodies (arrowheads in Fig. 1*I, K*), autophagosome-like double membrane vesicles (arrows in Fig. 1*K, J*), and autolysosomes (asterisks in Fig. 1*L*) in the motor neurons of the SALS patients, which were scarcely observed in the control patients.

Generation of the *dnc-1*-depleted *C. elegans* model

To examine the relationship between the loss of dynactin 1, the accumulation of autophagosomes, and motor neuron degeneration, we created a *dnc-1*-KD *C. elegans* model by transfecting *C. elegans* with a plasmid expressing an shRNA and GFP under the control of the motor neuron-specific *acr2* promoter (*dnc-1(RNAi)*). In the transgenic worms, GFP was expressed diffusely in ventral motor neurons (Fig. 2*A*). We confirmed the effect of RNA interference on the level of endogenous *dnc-1* mRNA using whole mount *in situ* hybridization. In the *control(RNAi)* worms, *dnc-1* expression was not altered by *shRNA::GFP* expression (Fig. 2*B*). Conversely, in the *dnc-1(RNAi)* worms, motor neurons expressing *shRNA::GFP* exhibited reduced or no expression of *dnc-1* (Fig. 2*B*). As shown in Fig. 2*C*, approximately 22 neurons were GFP-positive both in the *control(RNAi)* and *dnc-1(RNAi)* worms. The number of *dnc-1*-positive motor neurons was decreased by approximately 20 (*control(RNAi)* worms, 35.3±3.8; *dnc-1(RNAi)* worms, 15.9±9.8), suggesting that *dnc-1* was successfully knocked down in almost all the GFP-positive cells (Fig. 2*C, D*). Moreover, *dnc-1* expression was not affected in the head sensory neurons of the *dnc-1(RNAi)* worms, confirming the specificity of the promoter (Fig. 2*E*). Taking these results into account, in the following experiments, we selected the *dnc-1(RNAi)* and *control(RNAi)* worms expressing GFP in more than 30 motor neurons to avoid the influence of knockdown efficiency on the experimental results.

Motor dysfunction in motor neuron-specific *dnc-1*-KD *C. elegans*

The *dnc-1(RNAi)* worms demonstrated uncoordinated locomotion (Fig. 3*A*), which is a phenotype observed in *C. elegans* mutant models of motor neuronal defects [30,31]. Maturation of the worms resulted in the progressive aggravation of their uncoordinated locomotion, characterized by partial paralysis, slowed movement, and coiling. The feeding plate of the *dnc-1(RNAi)* worms appeared to be stagnated, as they only ate the food around themselves due to their decreased motility (Fig. 3*A*). As described in the Materials and Methods, we generated six lines of *dnc-1(RNAi)* worms: SBG7, 8, and 15 using shRNA1(101), and SBG20, 24, and 25 using shRNA2(2888). Survival analysis and body bend assays were performed using these six lines. Since these animals exhibited almost the same phenotype, SBG8 was employed for further analysis. Compared with the *control(RNAi)* worms, the *dnc-1(RNAi)* worms had a decreased life span (Fig. 3*B, C*) (11.4±4.4, 11.2±3.0, 13.4±4.0, and 14.3±3.3 days for *dnc-1(RNAi-1)*, *dnc-1(RNAi-2)*, *control(RNAi)*, and wild-type worms, respectively). *dnc-1(RNAi)* worms also exhibited significantly reduced bending and thrashing rates that declined with age

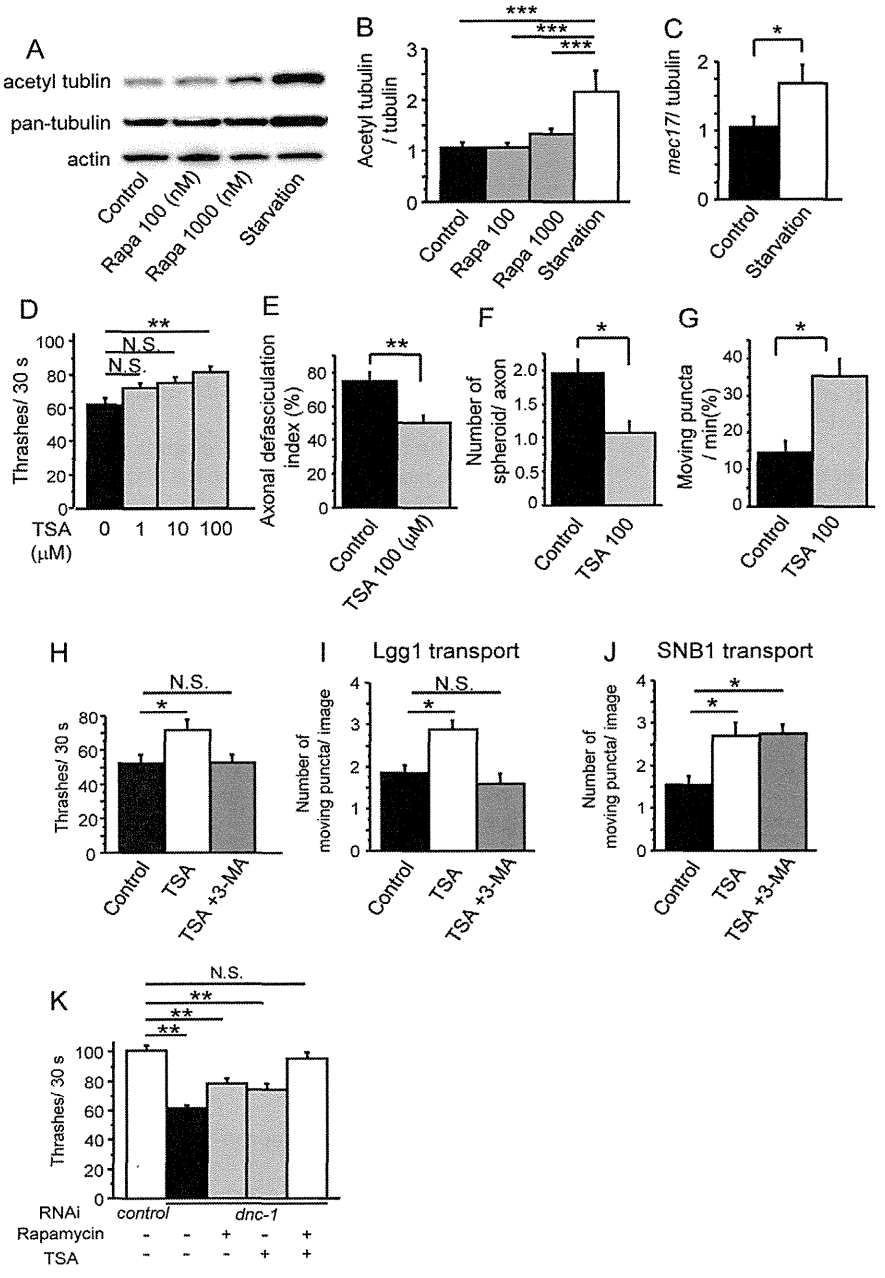

Figure 11. The effects of tubulin acetylation on the transport of autophagosome and neurodegeneration in the *dnc-1(RNAi)* worms. (*A, B*) Immunoblots of primary cultured cells using antibodies against acetylated tubulin, pan-tubulin, and actin (n = 5). (*C*) The mRNA levels of *mec17* measured by real-time RT-PCR. The data shown are ratios to the mRNA levels of *tba1*, the gene encoding alpha-tubulin. (*D*) Effect of trichostatin A (TSA) on the locomotor function of the *dnc-1(RNAi)* worms (n = 35 for each group). (*E–G*) Effect of TSA (100 μM) on the axonal degeneration of the *dnc-1(RNAi)* worms (*E, F*) and on autophagosome mobility (*G*) (n = 15 for each group). (*H*) The inhibition of autophagy by 3-MA (10 mM) negates the effect of TSA treatment on the motor function of the *dnc-1(RNAi)* worms (n = 35 for each group). (*I, J*) The number of moving puncta (*I*, Lgg1; *J*, SNB1) was counted using kymographs derived from *in vivo* time-lapse images (n = 20 images for each analysis). Treatment with 3-MA negates the effect of TSA treatment on the transport of Lgg1 (*I*), but not the transport of SNB1 (*J*). (*K*) Combination therapy of rapamycin (100 μM) and TSA (100 μM) has synergistic effects on the locomotive functions of the *dnc-1(RNAi)* worms (n = 35 for each group). Statistical analyses were performed by one-way ANOVA followed by the Bonferroni/Dunn post hoc test for (*B*), Dunnett's post hoc test (*D, H–K*), and Student's t test (*C, E–G*) (*p<0.05, **p<0.001, and ***p<0.0001). The error bars are S.E.M.
doi:10.1371/journal.pone.0054511.g011

(Fig. 3*D, E*). The thrashing speed of the *control(RNAi)* worms was slightly decreased compared with the wild-type worms, possibly due to the toxicity of GFP, as previously reported [32] (Fig. 3*E*). Although the toxicity of GFP was much less than that of *dnc-1* knockdown and not detectable in the bending assay, to exclude any effects of the fluorescent protein on our analysis, we compared

the *dnc-1(RNAi)* worms with the *control(RNAi)* worms, both of which express GFP at similar levels, in all experiments. We also performed a video capture analysis to visualize the movement trace of each worm and measure its average speed (Fig. 3*F, G*). The movement speed was dramatically decreased in the *dnc-1(RNAi)* worms compared with the *control(RNAi)* worms at an early adult stage.

Axonal degeneration is the early sign of neurodegeneration in the *dnc-1(RNAi)* worms

We then examined the morphological changes in the *dnc-1(RNAi)* worms using fluorescent microscopy. In normal worms, the ventral nerve cords were tightly fasciculated and the motor-neuron cell bodies (white asterisks in Fig. 4*A*) were round or ovoid. (Fig. 4*B, C*). By contrast, we found irregular shapes and defasciculation of the ventral nerve cord as well as axonal swellings, or spheroids, in the *dnc-1(RNAi)* worms at an early stage (Fig. 4*D*). At this early stage (4 days old), the cell bodies in the *dnc-1(RNAi)* worms seemed normal judging from their shape and structure (Fig. 4*D*). However, at a later adult stage (7 days old), axonal degeneration was exacerbated and morphological changes were also detected in the cell bodies (Fig. 4*E*). Axonal changes were occasionally observed in the *control(RNAi)* worms with aging, but they were less frequent and not as severe as in the *dnc-1(RNAi)* worms (Fig. 4*C*). Semi-quantification of the axonal and cell body changes showed that the axonal abnormalities were observed at day 4 and cell body deformation occurred at a later stage (Fig. 4*F*). Although some neurons exhibited an abnormal cell body shape at day 4, this change was only observed in the worms with axonal defasciculation (Fig. 4*G*), indicating that axonal degeneration occurs prior to cell body degeneration. Moreover, we also found that the severity of axonal defasciculation (i.e., the axonal defasciculation index) was correlated with locomotor dysfunction in the *dnc-1(RNAi)* worms (Fig. 4*H*). To clarify the time-course of the neuronal changes due to *dnc-1* depletion, we also examined the morphological change during the developmental stage. The acr2p::shRNA::GFP is not detectable before larval stage L1 (Fig. S1*A–C*). Furthermore, even after GFP is expressed, there was no alteration in morphology or motor phenotype during the larval stage (from L1 to L4, post natal days 1 and 2) (Fig. S1*C–E*). It was only after the worms became adult that the axonal degeneration and motor deficit appeared. Taken together, these findings suggest that the depletion of *dnc-1* induces the degeneration, rather than developmental defects, of motor neurons in *C. elegans*.

Further analysis via electron microscopy confirmed the axonal degeneration in the *dnc-1(RNAi)* worms (Fig. 5*C–F*). In the early degenerative stage, *dnc-1(RNAi)* worms first exhibited whorl like inclusions in axons with only a few morphological changes in their cell bodies (Fig. 5*C, D*) compared with *control(RNAi)* worms (Fig. 5*A, B*). In the later degenerative stage, strikingly abundant whorl-like inclusions and vacuoles, corresponding to degeneration and swelling of axons [21], were observed in axons and cell bodies (Fig. 5*E, F*).

Axonal transport defect in the *dnc-1(RNAi)* worms

Abnormalities in the localization and accumulation of synaptic vesicles were reported in a *C. elegans* model showing a defect in axonal transport [20]. To determine whether our *dnc-1(RNAi)* model exhibited defects in axonal transport, we used a fluorescently tagged synaptic vesicle marker composed of the *C. elegans* VAMP2/synaptobrevin protein fused to DsRed (SNB-1::DsRed), and examined the distribution of the dorsally located red puncta (Fig. 6*A*). In the dorsal nerve cord (the axons of the ventral motor neurons) of the *control(RNAi)* worms, SNB-1::DsRed puncta were regularly spaced, whereas the *dnc-1(RNAi)* worms exhibited a discontinuous and irregular distribution of the marker, including occasional clumps that may represent the accumulation of cargo proteins (Fig. 6*B*). Histograms of the distances between neighboring SNB-1 puncta displayed a broader curve in the *dnc-1(RNAi)* worms than in the *control(RNAi)* worms, suggesting some defect in axonal transport caused by the knockdown of *dnc-1* (Fig. 6*C, D*).

To demonstrate direct evidence of a defect in axonal transport in our transgenic worms, we monitored the movement of SNB-1 puncta by acquiring a series of time-lapse images. The resulting kymographs showed that puncta in the *dnc-1* KD worms were markedly static compared with those in the controls, confirming the disruption of axonal transport following the reduction of *dnc-1* in *C. elegans* (Fig. 6*E, F*, Movies S1, S2). To quantify the movement of SNB-1, we analyzed 20 kymographs from each strain. While there was no significant difference in the number of SNB-1 puncta between the *control(RNAi)* and *dnc-1(RNAi)* worms (Fig. 6*G*), the number of moving puncta (moving more than 2 μm) (Fig. 6*H*) and the ratio of moving puncta to total puncta (Fig. 6*I*) were significantly decreased in the *dnc-1(RNAi)* worms compared to the *control(RNAi)* worms ($p = 0.028$ and $p = 0.014$, respectively). The velocity of SNB-1 transport in the *dnc-1(RNAi)* worms was significantly lower than in the *control(RNAi)* worms ($p<0.0001$, Fig. 6*J*).

Impaired transport and accumulation of autophagosomes in the *dnc-1(RNAi)* worms

We next investigated the effects of *dnc-1* depletion on autophagy in *C. elegans*. Autophagosomes are cargo that moves bidirectionally along microtubules, powered by the kinesin family of motor proteins and dynein/dynactin complexes [11,12]. Altered autophagy has been observed in several neurodegenerative models, including the mutant *DCTN1* mouse model [9,16,33,34]. However, little is known about the relationship between the decreased levels of dynactin 1 and the alteration of autophagy. To clarify the effect of quantitative loss of DNC-1/dynactin 1 in the transport of autophagosomes, we performed live-cell imaging analyses of autophagosome transport in the axons of primary cultured motor neurons from the *dnc-1(RNAi)* and *control(RNAi)* worms that co-expressed DsRed-tagged Lgg1/ATG8, which is associated with the autophagic membrane, in ventral motor neurons under the control of the *acr2* promoter (Mizushima et al. [35]. This marker of autophagosomes is expressed diffusely in the ventral motor neurons (Fig. S2*A*) and forms distinct puncta when autophagosomes are formed (Fig. S2*B*) [36]. In the *control(RNAi)* neurons, the fluorescent Lgg1 vesicles moved toward and away from the cell body, suggesting that these vesicles are powered by anterograde and retrograde motors (Fig. 7*A*, Movie S3). By contrast, in the *dnc-1(RNAi)* worms, the autophagosomes were easily trapped where the axon was tight or curved, or at spheroids (Fig. 7*B*, Movie S4). This phenomenon was followed by the accumulation of autophagosomes distal to the trapped sites. Histograms showing the distribution of the velocity and distance of autophagosome movement demonstrated a significant loss of fast- and long-moving vesicles in the *dnc-1(RNAi)* cells compared with the *control(RNAi)* cells (Fig. 7*C, D*). The mean velocity and movement distance (run-length) were significantly decreased in the anterograde and retrograde directions in the *dnc-1(RNAi)* neurons ($p<0.0001$, $=0.0001$; velocity of anterograde, retrograde movements, respectively, and $p = 0.0045$, <0.0001; run-length of anterograde, retrograde movements, respectively) (Fig. 7*E, F*).

Next, we performed kymograph analysis of Lgg1::DsRed using *in vivo* time-lapse images (Fig. 8*A, B*, Movie S5, S6). Although the total number of Lgg1 puncta was significantly increased

($p<0.0001$) (Fig. 8*C*), the number (Fig. 8*D*) and the ratio of moving puncta (Fig. 8*E*) were significantly decreased in the *dnc-1(RNAi)* worms compared with the *control(RNAi)* worms ($p = 0.013$ and $p<0.0001$, respectively). The velocity of Lgg1 movement was also significantly decreased in the *dnc-1(RNAi)* worms ($p<0.0001$) (Fig. 8*F*). These results indicated that the *dnc-1* depletion resulted in the accumulation of untransported autophagosomes in the motor neurons.

We then investigated whether the accumulation of autophagosomes is related to the motor neuron degeneration. In the ventral nerve cord of the *dnc-1(RNAi)* worms, the number of Lgg1 puncta was significantly increased in comparison with the *control(RNAi)* worms ($p = 0.019$) (Fig. 8*G*), and the accumulation of autophagosomes was correlated with the axonal defasciculation index and locomotor function (Fig. 8*H, I*). We also explored the localization of Lgg1::DsRed in the distal ascending axon and observed Lgg1::DsRed accumulation in axonal spheroids (Fig. S2*C*), which is consistent with a previous report showing the abnormal accumulation of disorganized organelles and autophagosomes in axonal spheroids [37]. Electron microscopy showed that the accumulation of vesicular structures, including autophagosome-like vesicles and mitochondria, was observed in the proximal axons or cytoplasm of the *dnc-1(RNAi)* worms, although such accumulations were detected rarely in the axons of the *control(RNAi)* neurons (Fig. 8*J–L*).

We then treated the *control(RNAi)* worms with 3-MA, which inhibits the formation of autophagosomes (Fig. 9*A*). These worms showed the locomotory defects and axonal degeneration observed in the *dnc-1(RNAi)* worms, suggesting that the disrupted autophagy system is sufficient to cause the motor neuronal degeneration in this model (Fig. 9*B–E*). On the other hand, when we treated the *dnc-1(RNAi)* worms with 3-MA, worms did not exhibit a substantial change in the motor function or in the axonal integrity (Fig. 9*F–H*).

Starvation dramatically attenuates the motor deficits in the *dnc-1(RNAi)* worms by facilitating the axonal transport of autophagosomes

Autophagy is known to be activated by rapamycin, a specific inhibitor of the mTOR pathway [38]. Starvation is also a strong activator of autophagy; however, it also has other effects, e.g., activation of the mitogen-activated protein kinase (MAPK) pathway [39], stimulation of tubulin acetylation [40], and induction of sirtuin [41]. Both treatments have been used widely in many species, e.g., *Drosophila*, mouse, and *C. elegans*, to activate autophagy [42–44].

To study the effects of autophagy activators on axonal degeneration in *C. elegans*, we treated the *control(RNAi)* and *dnc-1(RNAi)* worms with rapamycin or starved them by food restriction, and investigated the changes in motor function via the liquid thrashing assay. Rapamycin and starvation are known to extend lifespan of *C. elegans* [42,45]. In the present study, we found that neither rapamycin nor starvation significantly altered the motor function of the *control(RNAi)* worms (Fig. 10*A*). In the *dnc-1(RNAi)* worms, rapamycin ameliorated the thrashing activity in a dose-dependent manner, although it showed only a limited effect even at the most effective dose (Fig. 10*A*). In contrast, starvation completely ameliorated the motor dysfunction of the *dnc-1(RNAi)* worms without affecting the efficiency of *dnc-1* knockdown (Fig. 10*A*, Fig. S3*A–C*). The formation of axonal spheroids was also significantly suppressed by starvation ($p = 0.001$) (Fig. 10*B, C*). Given the differential effects of rapamycin and starvation, we hypothesized that starvation not only increases the formation of autophagosomes but also increases their mobility in axons. Indeed, the frequency of autophagosome movement was increased by food restriction (Fig. 10*D*). To further confirm this hypothesis, we cultured primary motor neurons from the *dnc-1(RNAi)* worms in serum-depleted medium, and quantified the mobility of autophagosomes by monitoring the movement of DsRed-tagged Lgg1 in axons. As we expected, starvation significantly increased the speed and run-length of moving Lgg1 puncta, especially the retrograde run-length, in the *dnc-1(RNAi)* worms ($p<0.0001$) (Fig. 10*E, F*). Conversely, neurons treated with rapamycin showed no detectable change in the transport of autophagosomes (Fig. 10*E, F*). Histograms showing the distribution of the velocity and distance of autophagosome movement also demonstrated a significant increase of fast- and long-moving vesicles in the starved cells, especially in retrograde transport (Fig. 10*G, H*). For example, the percentage of vesicles that moved more than 8 μm retrogradely increased from 6.9% (*dnc-1(RNAi)* control) to 27.0% (*dnc-1(RNAi)* starvation), whereas the change was only from 12.7% to 19.7% in the anterograde direction (Fig. 10*H*).

Finally, we investigated how starvation stimulates the axonal transport of autophagosomes and assessed whether drugs that mimic the molecular mechanisms of starvation enhanced its effect. The acetylation of tubulin is known to stabilize microtubules and activate axonal transport by the subsequent recruitment of the molecular motors kinesin-1 and dynein/dynactin to microtubules [46,47]. Therefore, we assessed the acetylation state of alpha-tubulin in our cultured cell assay. Starvation increased the levels of acetylated tubulin, but this effect was not detected in cells treated with rapamycin (Fig. 11*A, B*). Moreover, real-time quantitative PCR demonstrated that starvation, but not rapamycin, significantly increased the mRNA levels of *mec-17*, an enzyme that acetylates tubulin in *C. elegans* [48] (Fig. 11*C*). Taken together, our results suggest the possibility that starvation mitigated axonal degeneration by activating autophagy and promoting the axonal transport of autophagosomes via the acetylation of tubulin in the *dnc-1(RNAi)* worms. To test this hypothesis, we examined the effects of TSA, an HDAC inhibitor that facilitates tubulin acetylation, on the phenotypes of the *dnc-1(RNAi)* worms. Although treatment with TSA did not exhibit substantial effects on the phenotype of the *control(RNAi)* worms (Fig. S4*A–C*), this treatment showed a significant effect on the locomotory function of the *dnc-1(RNAi)* worms in a dose-dependent manner, and attenuated the axonal degeneration without alteration of *dnc-1* knockdown efficiency (Fig. 11*D–F*, Fig. S3*A, B, and D*). As expected, TSA increased the mobility of autophagosomes (Fig. 11*G*). Interestingly, treatment with 3-MA dampened the effect of TSA on locomotion (Fig. 11*H*). On the contrary, the worms treated with both TSA and 3-MA showed decreased transport of autophagosomes without defects in the transport of synaptobrevin (Fig. 11*I, J*). Furthermore, we also examined the effect of combination therapy with rapamycin and TSA. Although treatment with rapamycin or TSA alone had limited effects in comparison with *control(RNAi)* worms, the combination of rapamycin and TSA had greater effects such that locomotion was restored in the worms treated with these two drugs to the levels observed in the *control(RNAi)* worms (Fig. 11*K*).

Discussion

In the present study, we generated a novel *C. elegans* model that mimics the down-regulation of dynactin 1 observed in the motor neurons of SALS patients. Using this model, we investigated whether the quantitative loss of DNC-1/dynactin 1 causes motor neuron degeneration. Our results showed that the knockdown of *dnc-1* caused progressive motor deficits in *C. elegans*, and the

pathological changes observed in this model shared several features with those seen in SALS patients, e.g., the axonal accumulation of membranous structures, such as mitochondria and autophagosomes, and motor neuron degeneration characterized by axonal degeneration including axonal spheroids. We also observed the disrupted transport of autophagosomes in the degenerated motor neurons of this model. Interestingly, our model exhibited adult-onset motor neuron degeneration even though the *shRNA::gfp* had already expressed in the larval stage. Given that the patients carrying mutant *DCTN1* and SALS patients exhibit an adult-onset motor neuron degeneration, it is possible that developing motor neurons are resistant to the disruption of DNC-1/dynactin 1. However, differentiated motor neurons may be vulnerable to the detrimental effects of dynactin 1 depletion, since they require more efficient transport system to maintain axonal homeostasis than developing neurons. Together, these findings indicate that this *dnc-1*-KD *C. elegans* model is a powerful tool for understanding the relationship between the disrupted transport of autophagosomes, neurodegeneration, and motor phenotype.

The mechanism of autophagosome accumulation in motor neurons harboring a motor protein abnormality was shown directly by our analysis of autophagosomal transport; namely, the knockdown of *dnc-1* decreased the transport of autophagosomes and shortened their run-length. Physiological cargoes typically use multiple motors, and their run-lengths are correlated with the number of coordinated motor proteins [49]. Our results showed that the knockdown of *dnc-1* reduced the speed and distance of retrograde transport by approximately half. These results are consistent with previous *in vitro* studies of dynein showing that the run-length of retrograde motor complexes is reduced by approximately half in cells lacking dynactin 1 [49,50]. Our data indicated that the knockdown of *dnc-1* also affected the anterograde transport of autophagosomes, which is consistent with previous reports showing that a defect in retrograde transport led to dysregulated movements in both directions [51,52].

The relationship between the decreased DNC-1/dynactin 1 levels, the increased number of autophagosomes, and axonal degeneration was confirmed by our observations that the *dnc-1(RNAi)* worms showed an abnormal accumulation of autophagosomes and that their locomotory defects and axonal degeneration were correlated with the accumulation of autophagosomes. Furthermore, the *control(RNAi)* worms treated with 3-MA, an inhibitor of autophagy, showed the same phenotype as the *dnc-1(RNAi)* worms, including defective locomotory function and degenerated axons. Taken together, our findings in the *dnc-1(RNAi) C. elegans* model provide direct evidence that the lack of DNC-1/dynactin 1 in dynein/dynactin motor complexes leads to slow, short-distance movements of autophagosomes, followed by their axonal accumulation, and neurodegeneration.

It is clinically important to determine whether the activation of autophagy could be an effective therapeutic strategy against neurodegenerative diseases, especially when the transport of autophagosomes is disrupted. In previous studies, the effects of rapamycin, which induces autophagosome formation [9], against models of neurodegeneration were controversial [53–55]. In the present study, rapamycin only slightly ameliorated the motor dysfunction of the *dnc-1(RNAi)* worms, although its effects were substantially enhanced by the addition of TSA which enhances the acetylation of tubulin. Given that tubulin acetylation was shown to stimulate axonal transport [47], our results suggest that combination therapy with rapamycin and TSA, attenuated the neurodegeneration and locomotory dysfunction of this model by facilitating the formation and axonal transport of autophagosomes.

Although it is still possible that the disrupted transport of other organelles such as mitochondria are also involved in the pathogenesis of motor neuron degeneration in the *dnc-1(RNAi)* worms, the observation that 3-MA, an inhibitor of autophagy, almost completely abrogated the benefit effects of TSA suggests a substantial role for autophagosomal transport in the functional maintenance of motor neurons. This view is further supported by the fact that the worms treated by both TSA and 3-MA showed the decreased transport of autophagosomes without defects in the transport of synaptobrevin.

In conclusion, we found that decreased levels of dynactin 1 in motor neurons induce neurodegeneration at least partially via the disruption of the axonal transport of autophagosomes. The therapeutic strategy we examined in this study could be expanded to other neurodegenerative disorders, since the accumulation of autophagosomes and disrupted axonal transport are common features of many neurodegenerative diseases. Future study is needed to explore the effectiveness and safety of the treatments that stimulate the transport of autophagosomes in the mammalian central nervous system.

Supporting Information

Figure S1 Expression pattern of *shRNA*::GFP and morphology of ventral motor neurons during embryonic and larval stage. (*A, B*) Representative confocal micro scopic image of *shRNA*::GFP expression during embryonic stages. GFP was not observed in the eggs even after delivery (asterisks in *A, B*). (*C–E*) GFP expression were observed in the ventral motor neurons (black arrows in *C*) from L1 (larval 1) stage of the worms. The ventral nerve axons (white arrows in *D, E*) did not exhibit abnormal changes such as axonal swellings or defasciculations during L1-4. Scale bars = 20 μm (*A–C*), 100 μm (low magnification image in *D, E*), or 50 μm (high magnification in *D, E*).
(TIF)

Figure S2 Expression pattern of the Lgg1::DsRed in the *control(RNAi)* worm and the *dnc-1(RNAi)* worm. (*A, B*) Representative fluorescent microscopic views of the Lgg1::DsRed in the ventral nerve cord of *control(RNAi)* worms (*A*) and *dnc-1(RNAi)* worms (*B*). The Lgg1 puncta (asteriscs in *B*) was abundant in the *dnc-1(RNAi)* worms (*B*). (*C*) Co-localization of DsRed and GFP fluorescence in the axonal spheroids (arrows) indicating that the autophagosomes (asteriscs) were accumulated in the axonal spheroids in the *dnc-1(RNAi)* worms. Scale bar = 10 μm (*A–C*).
(TIF)

Figure S3 Pharmacological treatment or starvation did not alter the efficiency of the *dnc-1* knock-down. (*A–D*) The representative image of GFP and *in situ* hybridization against *dnc-1* of ventral cholinergic motor neurons in the *conrol(RNAi)* (*A*) and *dnc-1(RNAi)* (*B*, no treatment; *C*, treated with starvation; *D*, treated with TSA). Scale bars = 10 μm.
(TIF)

Figure S4 Treatment with TSA did not alter the locomotor function or the axonal integrity of the *control(RNAi)* worms. (*A*) Effect of trichostatin A (TSA) on the locomotor function of the *control(RNAi)* worms (n = 35 for each group). (*B, C*) Effect of TSA (100 μM) on the axonal degeneration of the *dnc-1(RNAi)* worms (n = 15 for each group). Statistical analyses were performed using Student's t test.
(TIF)

Movie S1 Representative transport of SNB-1::DsRed puncta (red) in a ventral motor neurons from the control worm.
(MPEG)

Movie S2 Representative transport of SNB-1::DsRed puncta (red) in a ventral motor neurons from the *dnc-1* KD worm.
(MPEG)

Movie S3 Representative transport of Lgg1::DsRed puncta (red) in a primary motor neuron from the control worm.
(MPEG)

Movie S4 Representative transport of Lgg1::DsRed puncta (red) in a primary motor neuron from the *dnc-1* KD worm.
(MPEG)

Movie S5 Representatie transport of Lgg1::DsRed puncta (red) in a ventral motor neurons from the control worm.
(MPEG)

Movie S6 Representatie transport of Lgg1::DsRed puncta (red) in a ventral motor neurons from the *dnc-1* KD worm.
(MPEG)

Materials and Methods S1 Detailed materials and methods for *C. elegans* and human protocols.
(DOCX)

Author Contributions

Conceived and designed the experiments: KI MK FT IM GS. Performed the experiments: KI K. Kawai ZH YI YJ K. Kobayashi TK MW. Analyzed the data: KI K. Kawai MK. Contributed reagents/materials/analysis tools: TK K. Kobayashi IM. Wrote the paper: KI MK FT GS.

References

1. Klionsky DJ, Emr SD (2000) Autophagy as a regulated pathway of cellular degradation. Science 290: 1717–1721.
2. Hara T, Nakamura K, Matsui M, Yamamoto A, Nakahara Y, et al. (2006) Suppression of basal autophagy in neural cells causes neurodegenerative disease in mice. Nature 441: 885–889.
3. Komatsu M, Waguri S, Chiba T, Murata S, Iwata J, et al. (2006) Loss of autophagy in the central nervous system causes neurodegeneration in mice. Nature 441: 880–884.
4. Ravikumar B, Acevedo-Arozena A, Imarisio S, Berger Z, Vacher C, et al. (2005) Dynein mutations impair autophagic clearance of aggregate-prone proteins. Nat Genet 37: 771–776.
5. Komatsu M, Wang QJ, Holstein GR, Friedrich VL Jr., Iwata J, et al. (2007) Essential role for autophagy protein Atg7 in the maintenance of axonal homeostasis and the prevention of axonal degeneration. Proc Natl Acad Sci U S A 104: 14489–14494.
6. Anglade P, Vyas S, Javoy-Agid F, Herrero MT, Michel PP, et al. (1997) Apoptosis and autophagy in nigral neurons of patients with Parkinson's disease. Histol Histopathol 12: 25–31.
7. Sapp E, Schwarz C, Chase K, Bhide PG, Young AB, et al. (1997) Huntingtin localization in brains of normal and Huntington's disease patients. Ann Neurol 42: 604–612.
8. Sasaki S (2011) Autophagy in spinal cord motor neurons in sporadic amyotrophic lateral sclerosis. J Neuropathol Exp Neurol 70: 349–359.
9. Yu WH, Cuervo AM, Kumar A, Peterhoff CM, Schmidt SD, et al. (2005) Macroautophagy--a novel Beta-amyloid peptide-generating pathway activated in Alzheimer's disease. J Cell Biol 171: 87–98.
10. Li L, Zhang X, Le W (2008) Altered macroautophagy in the spinal cord of SOD1 mutant mice. Autophagy 4: 290–293.
11. Yang Y, Xu K, Koike T, Zheng X (2008) Transport of autophagosomes in neurites of PC12 cells during serum deprivation. Autophagy 4: 243–245.
12. Katsumata K, Nishiyama J, Inoue T, Mizushima N, Takeda J, et al. (2010) Dynein- and activity-dependent retrograde transport of autophagosomes in neuronal axons. Autophagy 6: 378–385.
13. Jiang YM, Yamamoto M, Tanaka F, Ishigaki S, Katsuno M, et al. (2007) Gene expressions specifically detected in motor neurons (dynactin 1, early growth response 3, acetyl-CoA transporter, death receptor 5, and cyclin C) differentially correlate to pathologic markers in sporadic amyotrophic lateral sclerosis. J Neuropathol Exp Neurol 66: 617–627.
14. Puls I, Jonnakuty C, LaMonte BH, Holzbaur EL, Tokito M, et al. (2003) Mutant dynactin in motor neuron disease. Nat Genet 33: 455–456.
15. Levy JR, Sumner CJ, Caviston JP, Tokito MK, Ranganathan S, et al. (2006) A motor neuron disease-associated mutation in p150Glued perturbs dynactin function and induces protein aggregation. J Cell Biol 172: 733–745.
16. Laird FM, Farah MH, Ackerley S, Hoke A, Maragakis N, et al. (2008) Motor neuron disease occurring in a mutant dynactin mouse model is characterized by defects in vesicular trafficking. J Neurosci 28: 1997–2005.
17. Katsuno M, Adachi H, Kume A, Li M, Nakagomi Y, et al. (2002) Testosterone reduction prevents phenotypic expression in a transgenic mouse model of spinal and bulbar muscular atrophy. Neuron 35: 843–854.
18. Brenner S (1974) The genetics of Caenorhabditis elegans. Genetics 77: 71–94.
19. Takada T, Iida K, Sasaki H, Taira M, Kimura H (2005) Expression of ADP-ribosylation factor (ARF)-like protein 6 during mouse embryonic development. Int J Dev Biol 49: 891–894.
20. Koushika SP, Schaefer AM, Vincent R, Willis JH, Bowerman B, et al. (2004) Mutations in Caenorhabditis elegans cytoplasmic dynein components reveal specificity of neuronal retrograde cargo. J Neurosci 24: 3907–3916.
21. Kraemer BC, Zhang B, Leverenz JB, Thomas JH, Trojanowski JQ, et al. (2003) Neurodegeneration and defective neurotransmission in a Caenorhabditis elegans model of tauopathy. Proc Natl Acad Sci U S A 100: 9980–9985.
22. Miyara A, Ohta A, Okochi Y, Tsukada Y, Kuhara A, et al. (2011) Novel and Conserved Protein Macoilin Is Required for Diverse Neuronal Functions in Caenorhabditis elegans. PLoS Genet 7: e1001384.
23. Lewis JA, Fleming JT (1995) Basic culture methods. Methods Cell Biol 48: 3–29.
24. Strange K, Christensen M, Morrison R (2007) Primary culture of Caenorhabditis elegans developing embryo cells for electrophysiological, cell biological and molecular studies. Nat Protoc 2: 1003–1012.
25. Stiernagle T (2006) Maintenance of C. elegans. WormBook: 1–11.
26. Paredez AR, Persson S, Ehrhardt DW, Somerville CR (2008) Genetic evidence that cellulose synthase activity influences microtubule cortical array organization. Plant Physiol 147: 1723–1734.
27. Hall DH, Gu G, Garcia-Anoveros J, Gong L, Chalfie M, et al. (1997) Neuropathology of degenerative cell death in Caenorhabditis elegans. J Neurosci 17: 1033–1045.
28. Ishigaki S, Liang Y, Yamamoto M, Niwa J, Ando Y, et al. (2002) X-Linked inhibitor of apoptosis protein is involved in mutant SOD1-mediated neuronal degeneration. J Neurochem 82: 576–584.
29. Katsuno M, Adachi H, Doyu M, Minamiyama M, Sang C, et al. (2003) Leuprorelin rescues polyglutamine-dependent phenotypes in a transgenic mouse model of spinal and bulbar muscular atrophy. Nat Med 9: 768–773.
30. Thomas JH (1990) Genetic analysis of defecation in Caenorhabditis elegans. Genetics 124: 855–872.
31. McIntire SL, Garriga G, White J, Jacobson D, Horvitz HR (1992) Genes necessary for directed axonal elongation or fasciculation in C. elegans. Neuron 8: 307–322.
32. Comley LH, Wishart TM, Baxter B, Murray LM, Nimmo A, et al. (2011) Induction of cell stress in neurons from transgenic mice expressing yellow fluorescent protein: implications for neurodegeneration research. PLoS One 6.
33. Sikorska B, Liberski PP, Giraud P, Kopp N, Brown P (2004) Autophagy is a part of ultrastructural synaptic pathology in Creutzfeldt-Jakob disease: a brain biopsy study. Int J Biochem Cell Biol 36: 2563–2573.
34. Nixon RA, Wegiel J, Kumar A, Yu WH, Peterhoff C, et al. (2005) Extensive involvement of autophagy in Alzheimer disease: an immuno-electron microscopy study. J Neuropathol Exp Neurol 64: 113–122.
35. Mizushima N, Yoshimori T, Levine B (2010) Methods in mammalian autophagy research. Cell 140: 313–326.
36. Melendez A, Levine B (2009) Autophagy in C. elegans. WormBook: 1–26.
37. Ohara S, Ukita Y, Ninomiya H, Ohno K (2004) Axonal dystrophy of dorsal root ganglion sensory neurons in a mouse model of Niemann-Pick disease type C. Exp Neurol 187: 289–298.
38. Noda T, Ohsumi Y (1998) Tor, a phosphatidylinositol kinase homologue, controls autophagy in yeast. J Biol Chem 273: 3963–3966.
39. You YJ, Kim J, Cobb M, Avery L (2006) Starvation activates MAP kinase through the muscarinic acetylcholine pathway in Caenorhabditis elegans pharynx. Cell Metab 3: 237–245.
40. Geeraert C, Ratier A, Pfisterer SG, Perdiz D, Cantaloube I, et al. (2010) Starvation-induced hyperacetylation of tubulin is required for the stimulation of autophagy by nutrient deprivation. J Biol Chem 285: 24184–24194.
41. Morselli E, Maiuri MC, Markaki M, Megalou E, Pasparaki A, et al. (2010) Caloric restriction and resveratrol promote longevity through the Sirtuin-1-dependent induction of autophagy. Cell Death Dis 1: e10.
42. Hansen M, Chandra A, Mitic LL, Onken B, Driscoll M, et al. (2008) A role for autophagy in the extension of lifespan by dietary restriction in C. elegans. PLoS Genet 4: e24.

43. Sarkar S, Krishna G, Imarisio S, Saiki S, O'Kane CJ, et al. (2008) A rational mechanism for combination treatment of Huntington's disease using lithium and rapamycin. Hum Mol Genet 17: 170–178.
44. Harrison DE, Strong R, Sharp ZD, Nelson JF, Astle CM, et al. (2009) Rapamycin fed late in life extends lifespan in genetically heterogeneous mice. Nature 460: 392–395.
45. Robida-Stubbs S, Glover-Cutter K, Lamming DW, Mizunuma M, Narasimhan SD, et al. (2012) TOR signaling and rapamycin influence longevity by regulating SKN-1/Nrf and DAF-16/FoxO. Cell Metab 15: 713–724.
46. Reed NA, Cai D, Blasius TL, Jih GT, Meyhofer E, et al. (2006) Microtubule acetylation promotes kinesin-1 binding and transport. Curr Biol 16: 2166–2172.
47. Dompierre JP, Godin JD, Charrin BC, Cordelieres FP, King SJ, et al. (2007) Histone deacetylase 6 inhibition compensates for the transport deficit in Huntington's disease by increasing tubulin acetylation. J Neurosci 27: 3571–3583.
48. Akella JS, Wloga D, Kim J, Starostina NG, Lyons-Abbott S, et al. (2010) MEC-17 is an alpha-tubulin acetyltransferase. Nature 467: 218-222.
49. Ori-McKenney KM, Xu J, Gross SP, Vallee RB (2010) A cytoplasmic dynein tail mutation impairs motor processivity. Nat Cell Biol 12: 1228–1234.
50. Ross JL, Wallace K, Shuman H, Goldman YE, Holzbaur EL (2006) Processive bidirectional motion of dynein-dynactin complexes in vitro. Nat Cell Biol 8: 562–570.
51. Haghnia M, Cavalli V, Shah SB, Schimmelpfeng K, Brusch R, et al. (2007) Dynactin is required for coordinated bidirectional motility, but not for dynein membrane attachment. Mol Biol Cell 18: 2081–2089.
52. Welte MA (2010) Bidirectional transport: matchmaking for motors. Curr Biol 20: R410–413.
53. Caccamo A, Majumder S, Deng JJ, Bai Y, Thornton FB, et al. (2009) Rapamycin rescues TDP-43 mislocalization and the associated low molecular mass neurofilament instability. J Biol Chem 284: 27416–27424.
54. Spilman P, Podlutskaya N, Hart MJ, Debnath J, Gorostiza O, et al. (2010) Inhibition of mTOR by rapamycin abolishes cognitive deficits and reduces amyloid-beta levels in a mouse model of Alzheimer's disease. PLoS One 5: e9979.
55. Zhang X, Li L, Chen S, Yang D, Wang Y, et al. (2011) Rapamycin treatment augments motor neuron degeneration in SOD1 (G93A) mouse model of amyotrophic lateral sclerosis. Autophagy 7.

nature COMMUNICATIONS

ARTICLE

Received 17 Sep 2012 | Accepted 20 Dec 2012 | Published 29 Jan 2013

DOI: 10.1038/ncomms2417

Heat shock factor-1 influences pathological lesion distribution of polyglutamine-induced neurodegeneration

Naohide Kondo[1], Masahisa Katsuno[1], Hiroaki Adachi[1], Makoto Minamiyama[1], Hideki Doi[1], Shinjiro Matsumoto[1], Yu Miyazaki[1], Madoka Iida[1], Genki Tohnai[1], Hideaki Nakatsuji[1], Shinsuke Ishigaki[1], Yusuke Fujioka[1], Hirohisa Watanabe[1], Fumiaki Tanaka[1], Akira Nakai[2] & Gen Sobue[1]

A crucial feature of adult-onset neurodegenerative diseases is accumulation of abnormal protein in specific brain regions, although the mechanism underlying this pathological selectivity remains unclear. Heat shock factor-1 is a transcriptional regulator of heat shock proteins, molecular chaperones that abrogate neurodegeneration by refolding and solubilizing pathogenic proteins. Here we show that heat shock factor-1 expression levels are associated with the accumulation of pathogenic androgen receptor in spinal and bulbar muscular atrophy, a polyglutamine-induced neurodegenerative disease. In heterozygous *heat shock factor-1*-knockout spinal and bulbar muscular atrophy mice, abnormal androgen receptor accumulates in the cerebral visual cortex, liver and pituitary, which are not affected in their genetically unmodified counterparts. The depletion of *heat shock factor-1* also expands the distribution of pathogenic androgen receptor accumulation in other neuronal regions. Furthermore, lentiviral-mediated delivery of heat shock factor-1 into the brain of spinal and bulbar muscular atrophy mice topically suppresses the pathogenic androgen receptor accumulation and neuronal atrophy. These results suggest that heat shock factor-1 influences the pathological lesion selectivity in spinal and bulbar muscular atrophy.

[1] Department of Neurology, Nagoya University Graduate School of Medicine, Nagoya 466-8550, Japan. [2] Department of Biochemistry and Molecular Biology, Yamaguchi University School of Medicine, Ube 755-8505, Japan. Correspondence and requests for materials should be addressed to M.K. (email: ka2no@med.nagoya-u.ac.jp).

Heat shock proteins (Hsps), including Hsp70 and Hsp40, are stress-induced molecular chaperones that have important roles in maintaining correct folding, the assembly of newly synthesized proteins and the intracellular transport of proteins[1,2]. There are various lines of evidence indicating that Hsps abrogate neurodegeneration by refolding and solubilizing pathogenic proteins[3,4]. Particularly, Hsp70 facilitates the proteasomal degradation of abnormal proteins and thereby ameliorates neuronal damage in cellular and animal models of adult-onset neurodegenerative disorders, including Alzheimer's disease, amyotrophic lateral sclerosis and Huntington' disease (HD)[5–7] and other polyglutamine diseases caused by the expansion of a genomic CAG repeat[8–10]. Among several molecules that control the expression of Hsps, heat shock factor-1 (Hsf-1) is shown to strongly regulate the expression of Hsp70 by activating its promoter[11,12].

To develop effective treatments for neurodegenerative disorders, it is important to elucidate the molecular mechanism by which only specific cells are affected, despite the broad expression of the disease-causing mutant genes. The selectivity of the pathogenic lesions in neurodegenerative diseases may be influenced by several factors. For example, the length of the CAG triplet repeat in the causative gene influences the distribution of pathological lesions of spinocerebellar ataxia type 7 and dentatorubral pallidoluysian atrophy[13,14]. Given that the length of the polyglutamine tract increases the propensity of the protein to aggregate, the pathological lesion selectivity of spinocerebellar ataxia type 7 appears to be influenced by the biological properties of the causative protein[15]. Alternatively, the expression of molecules that interact with the disease-causing proteins, such as PQBP-1 and Rhes, is also associated with the distribution of selective neuronal cell loss in polyglutamine diseases[16,17]. Furthermore, transcriptional factors such as nuclear transcription factor Y subunit alpha (NF-YA) and p53 were shown to, at least partially, determine the vulnerability of cells to polyglutamine-expanded proteins by regulating the expression of Hsps in cellular models of HD[18,19].

The accumulation of polyglutamine-expanded proteins is detected histopathologically as diffuse nuclear staining or as intraneuronal inclusion bodies, the distribution of which corresponds to that of pathological involvement and symptomatic phenotypes[20,21]. The intranuclear accumulation of disease-causing misfolded proteins is thought to trigger neurodegeneration by various mechanisms such as transcriptional dysregulation, impairment of axonal transport and mitochondrial dysfunction[22–24]. This view is supported by animal studies showing that the prevention of pathogenic protein accumulation successfully rescues the phenotype in model mice of polyglutamine diseases[25–28].

Here, we investigated the role of Hsf-1 in pathogenic lesion selectivity in spinal and bulbar muscular atrophy (SBMA), an adult-onset motor neuron disease caused by the expansion of a CAG repeat in the gene coding androgen receptor (AR)[29–31]. This disease affects susceptible regions, such as spinal anterior horn, brainstem and pancreas, despite the ubiquitous expression of the causative protein[32]. In the present study, we found that the heterozygous knockout of *Hsf-1* in SBMA model mice led to the extended distribution of pathogenic AR accumulation in neuronal and non-neuronal tissues as well as exacerbated neuromuscular phenotype, whereas the lentiviral overexpression of HSF-1 locally precludes pathogenic AR accumulation and neuronal atrophy in the brain of the SBMA mice.

Results

Hsf-1 levels are associated with pathogenic AR accumulation. To examine whether the expression levels of Hsf-1 are associated with the distribution of pathogenic AR accumulation in SBMA, we performed immunohistochemistry on the central nervous system (CNS) of a transgenic SBMA mouse model carrying human AR with 97 CAGs (AR-97Q). In this model animal, the full-length human AR was expressed ubiquitously (Supplementary Fig. S1a). The results showed that low expression levels of Hsf-1 were associated with a high frequency of pathogenic AR accumulation (Fig. 1a,b). For example, the accumulation of pathogenic AR is frequently observed in spinal motor neurons that show weak immunoreactivity for Hsf-1. In contrast, neurons in the cerebral cortex and striatum, most of which are Hsf-1-positive, were rarely stained with 1C2, a specific antibody against the expanded polyglutamine tract. In the cerebellum of AR-97Q mice, there was a scarce accumulation of pathogenic AR in Purkinje cells, where Hsf-1 was expressed at a high level. Conversely, there were abundant 1C2-positive cells in the cerebellar granular cell layer, which showed scarce immunoreactivity for Hsf-1 (Fig. 1a). There was little difference in the expression pattern of Hsf-1 between AR-97Q and wild-type mice, except for the spinal anterior horn, where the nuclear expression of Hsf-1 was decreased in AR-97Q mice compared with wild-type mice (Fig. 1a). Quantitative analysis of the relationship between the expression levels of Hsf-1 and the frequency of 1C2-positive cells in various parts of the CNS confirmed that higher expression levels of Hsf-1 are associated with the reduced accumulation of pathogenic AR (Fig. 1b). This relationship, however, was not clearly observed for Nfya, p53, TATA box-binding protein (Tbp) or Sp1, which are other potential inducers of Hsp70 (Supplementary Fig. S1b,c). These findings led us to focus on Hsf-1 as a possible regulator of the pathogenic lesion selectivity, especially in the CNS, of the SBMA model mouse.

Previous studies showed that AR-97Q mice show pathogenic AR aggregation in non-neuronal tissues, such as the heart, lung, pancreas and skeletal muscle, in addition to the CNS[25]. To examine whether the expression levels of Hsf-1 are also associated with pathogenic AR accumulation outside the CNS, we performed immunohistochemistry using anti-Hsf-1 and 1C2 antibodies on non-neuronal tissues of the AR-97Q mice. The results demonstrated that a similar relationship as seen in CNS was observed in the pancreas, liver and testis. There was unequivocal pathogenic AR accumulation in the pancreas, where Hsf-1 is expressed at a low level (Supplementary Fig. S1d). In contrast, no visible pathogenic AR accumulation was observed in the liver or testis, where Hsf-1 is expressed at a relatively high level (Supplementary Fig. S1d).

We further verified this relationship in autopsied specimens from SBMA patients. 1C2-positive cells were frequently detected in spinal motor neurons and pancreatic islet cells, where HSF-1 is expressed at a low level, compared with control subjects. In contrast, there were no 1C2-stained cells in the neuronal and non-neuronal tissues in which HSF-1 was expressed at a high level (Supplementary Fig. S2a,b).

Taken together, these results indicate that high expression levels of Hsf-1 are associated with reduced pathogenic AR accumulation in neuronal and non-neuronal tissues of the SBMA mouse model and SBMA patients.

***Hsf-1* depletion expands distribution of AR accumulation.** To clarify whether low expression levels of Hsf-1 have a causative role in the accumulation of pathogenic AR *in vivo*, we depleted *Hsf-1* in AR-97Q mice by crossing them with heterozygous *Hsf-1*-knockout mice[33]. As *Hsf-1*-null AR-97Q (AR-97Q Tg/−, *Hsf-1* −/−) mice were not obtained, presumably owing to their early death during embryonic development, we performed immunohistochemistry on various tissues from wild-type

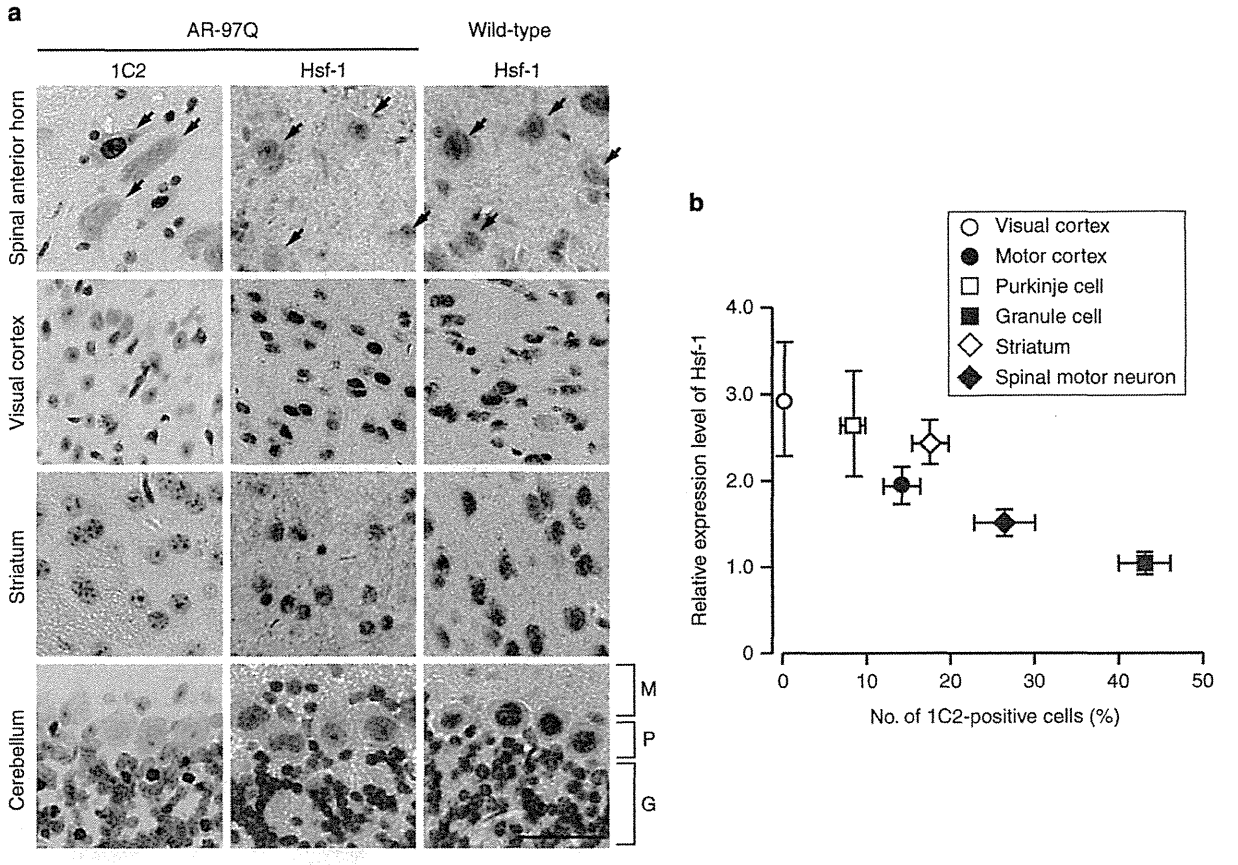

Figure 1 | Hsf-1 expression is associated with pathogenic AR accumulation. (**a**) Immunohistochemistry for Hsf-1 and expanded polyglutamine (1C2) in the spinal anterior horn, visual cortex, striatum and cerebellum from wild-type and AR-97Q mice (13 weeks old). Arrows indicate motor neurons within the spinal anterior horn. M, molecular layer; P, Purkinje cell layer; G, granular layer. (**b**) Quantification of the relationship between the nuclear immunoreactivity of Hsf-1 and the frequency of 1C2-positive cells in different parts of the CNS. More than 500 neurons in each part from three brains were analysed (**b**). Error bars indicate s.e.m. (**b**). Scale bars, 50 μm (**a**).

(AR-97Q −/−, *Hsf-1* +/+), AR-97Q (AR-97Q Tg/−, *Hsf-1* +/+) and heterozygous *Hsf-1*-knockout AR-97Q (AR-97Q Tg/−, *Hsf-1* +/−) mice, to examine whether Hsf-1 inactivation expands the distribution of pathogenic AR accumulation. The nuclear accumulation of pathogenic AR is not detected in the liver and pituitary gland of AR-97Q mice, even at an advanced stage (Supplementary Fig. S3). Surprisingly, we observed the nuclear accumulation of pathogenic AR in the liver of the heterozygous *Hsf-1*-knockout SBMA mice (Fig. 2a). Quantitative analysis showed that 1.40 ± 0.35% (1.0–2.1) of hepatocytes were positive for 1C2 in the *Hsf-1*-depleted AR-97Q mice, while no positive cells were observed in the AR-97Q mice ($n = 3$ per group). To confirm the effects of *Hsf-1* depletion on the metabolism of pathogenic AR, we performed immunoblotting of the liver samples using an anti-AR antibody. The results revealed that the expression level of AR monomer, which appears to be one of the toxic species of polyglutamine protein[34], was increased by the heterozygous knockout of *Hsf-1* in the liver of AR-97Q mice (Fig. 2b,c). Insoluble high-molecular-weight AR complexes, which may have a protective property, were not detected in the liver of either type of mice, presumably because of the relatively low expression levels of AR in this tissue.

To assess whether the accumulation of pathogenic AR due to *Hsf-1* depletion impairs liver function, we performed histology and blood tests on each mouse group. The serum levels of liver enzymes, such as aspartate aminotransferase and alanine aminotransferase, which are indicative of liver dysfunction, were significantly elevated in heterozygous *Hsf-1*-knockout AR-97Q mice compared with the genetically unmodified AR-97Q mice (Fig. 2d,e), while this was not the case for wild-type mice (Fig. 2f,g). Furthermore, immunohistochemistry demonstrated that the liver became atrophied in the heterozygous *Hsf-1*-knockout AR-97Q mice, but not in their wild-type counterparts (Fig. 2h–j). Similarly, pathogenic AR accumulation was also detected in the pituitary gland of the heterozygous *Hsf-1*-knockout SBMA mice (Fig. 2a). A total of 0.67 ± 0.17% (0.5–1.0) of the cells in the pituitary gland of the heterozygous *Hsf-1*-knockout AR-97Q mice exhibited the nuclear accumulation of pathogenic AR, although there were no 1C2-positive cells in the pituitary gland of genetically unmodified AR-97Q mice ($n = 3$ per group). These findings indicate that Hsf-1 prevents the accumulation of pathogenic AR in the liver and pituitary gland of AR-97Q mice.

A similar phenomenon was observed in certain parts of the CNS in AR-97Q mice. Interestingly, the accumulation of pathogenic AR was detected in the cerebral visual cortex of heterozygous *Hsf-1*-knockout SBMA mice (Fig. 3a), where the accumulation of pathogenic AR was not observed in the AR-97Q mice, even at an advanced stage (Supplementary Fig. S3). Furthermore, the heterozygous knockout of *Hsf-1* also augmented the accumulation of pathogenic AR in spinal motor neurons and Purkinje cells as well as the neurons of the striatum

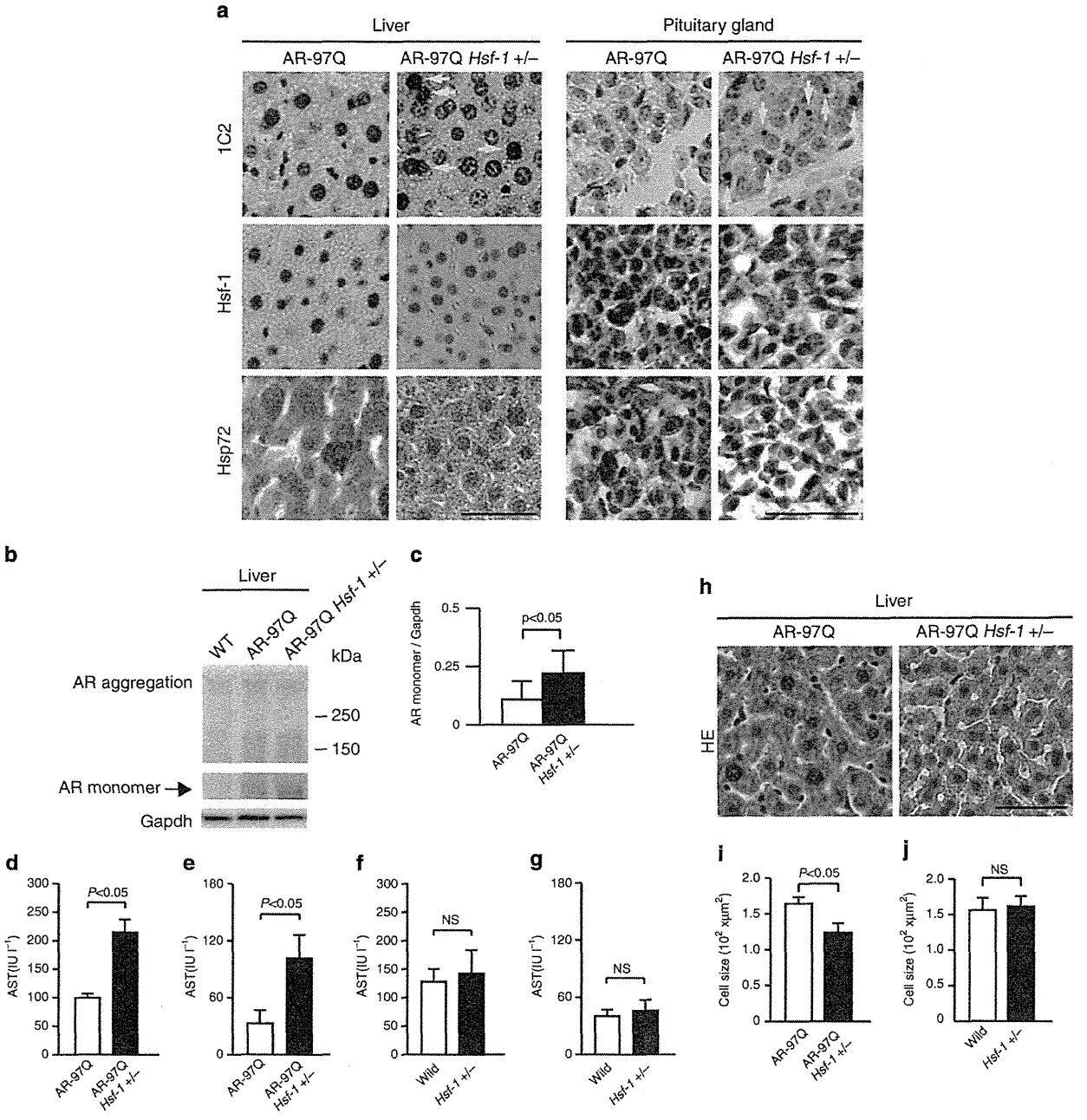

Figure 2 | Pathogenic AR accumulates in the liver and pituitary gland of heterozygous *Hsf-1*-knockout AR-97Q mice. (**a**) Immunohistochemistry of AR-97Q and *Hsf-1*-knockout AR-97Q mice using anti-Hsf-1, anti-Hsp72 and anti-polyglutamine (1C2) antibodies (13 weeks old). The *Hsf-1*-knockout AR-97Q mice showed the nuclear accumulation of pathogenic AR (yellow arrows) and decreased levels of Hsf-1 and Hsp72, an inducible form of Hsp70, in the liver and pituitary gland. (**b**) Immunoblotting for AR in wild-type, AR-97Q and *Hsf-1*-knockout AR-97Q mice (13 weeks old). (**c**) Quantification of immunoblotting revealed that the expression levels of AR monomer were upregulated in the liver of heterozygous *Hsf-1*-knockout AR-97Q mice. Unpaired *t*-test, $n=3$. (**d**–**g**) Blood tests revealed that the liver enzyme levels, including aspartate aminotransferase (AST) (**d**) and alanine aminotransferase (ALT) (**e**), were elevated in heterozygous *Hsf-1*-knockout AR-97Q mice compared with AR-97Q mice (13 weeks old). There were no significant differences in the levels of AST (**f**) and ALT (**g**) between wild-type and heterozygous *Hsf-1*-knockout mice (13 weeks old). (**h**) Haematoxylin-eosin staining of the liver of heterozygous *Hsf-1*-knockout and genetically unmodified AR-97Q mice (13 weeks old). (**i**) Quantitative analysis showed that the size of hepatocytes was reduced in heterozygous *Hsf-1*-knockout AR-97Q mice compared with AR-97Q mice. (**j**) Depletion of *Hsf-1* did not alter the size of hepatocytes in wild-type mice. Unpaired *t*-test ($n=4$) (**d**–**g**). More than 1,000 cells from three livers were analysed in each group, unpaired *t*-test. (**i**,**j**). Error bars indicate s.e.m. (**c**–**g**,**i**,**j**). Scale bars, 50 μm (**a**,**h**). NS, not significant.

through Hsp70 downregulation (Fig. 3a and Supplementary Fig. S4a). Quantitative analysis of the change in the relationship between the Hsf-1 expression levels and the frequency of 1C2-positive cells confirmed that the accumulation of pathogenic AR was significantly increased by the heterozygous depletion of Hsf-1 (Fig. 3b–e). Although pathogenic AR mainly

accumulated in the fifth and sixth layers of the cerebral motor cortex in the AR-97Q mice, where the expression levels of Hsf-1 are relatively lower than in the other layers, the distribution of pathogenic AR accumulation was expanded to the second and third layers in the heterozygous *Hsf-1*-knockout AR-97Q mice (Fig. 3f). The heterozygous knockout of *Hsf-1* also altered the distribution and frequency of pathogenic AR accumulation in neuronal and non-neuronal tissues in the AR-97Q mice (Supplementary Fig. S4b and Supplementary Table S1). To verify the impact of *Hsf-1* depletion upon the pathogenic AR aggregations, we next analysed immunoblots of the spinal cord, cerebral cortex, striatum and cerebellum using an anti-AR antibody. The findings showed that the amount of smearing AR protein, which corresponds to the toxic oligomers, was increased by the heterozygous depletion of *Hsf-1* in each part of the CNS of the AR-97Q mice (Fig. 3g–i). These findings suggest that Hsf-1 expression levels influence the degree of pathogenic AR accumulation in the SBMA mouse model.

***Hsf-1* depletion aggravates neurodegeneration in SBMA mice.** To examine whether the decreased expression levels of Hsf-1 leads to increased motor neuronal damage in the SBMA mouse model, we analysed the effects of *Hsf-1* depletion on the neurological and histopathological phenotypes of AR-97Q mice. The results demonstrated that muscle atrophy was enhanced in the *Hsf-1*-knockout AR-97Q mice compared with the genetically unmodified AR-97Q mice (Fig. 4a and Supplementary Movie 1). Footprint analysis showed that the stride length was shortened and the paws were dragged in the heterozygous *Hsf-1*-knockout AR-97Q mice (Fig. 4b,c). The heterozygous knockout of *Hsf-1* in AR-97Q mice also shortened their lifespan and decreased their body weight, and also exacerbated muscle weakness, as measured using grip power and the rotarod task (Fig. 4d–g). To exclude nonspecific effects of *Hsf-1* depletion on the motor phenotypes of wild-type mice, we investigated the lifespan and motor function of heterozygous *Hsf-1*-knockout wild-type mice (Supplementary Fig. S5a–d). The results showed that the heterozygous knockout of *Hsf-1* had no influence on the lifespan, body weight or motor function of wild-type mice, suggesting that the deleterious effects of *Hsf-1* depletion are disease-specific phenomena.

To investigate the neuropathological changes underlying the phenotypic aggravation and the increase of pathogenic 1C2-positive neuronal cells, we performed immunohistochemistry on the spinal anterior horn, cerebral cortex, striatum and cerebellum of heterozygous *Hsf-1*-knockout and genetically unmodified AR-97Q mice using antibodies against choline acetyl transferase (ChAT), NeuN and calbindin. The results showed that neurons in each part of the CNS were atrophied in the *Hsf-1*-knockout AR-97Q mice (Fig. 5a–h). Western blot analysis confirmed the decreased levels of ChAT, a functional marker of spinal motor neurons, in the heterozygous *Hsf-1*-knockout AR-97Q mice (Fig. 5i,j).

To analyse the effects of *Hsf-1* depletion on the denervation at neuromuscular junctions (NMJs) of AR-97Q mice, we performed immunofluorescent staining of NMJs using α-bungarotoxin together with antibodies against synaptophysin and phospho neurofilament (Fig. 5k). Quantitative analysis showed that the frequency of denervation at NMJ is increased in the heterozygous *Hsf-1*-knockout SBMA mice compared with the AR-97Q mice (Fig. 5l). In addition, immunohistochemistry and immunoblot analysis using an antibody against glial fibrillary acid protein (GFAP) showed increased immunoreactivity in the anterior horn of the spinal cord of the heterozygous *Hsf-1*-knockout SBMA mice compared with AR-97Q mice, indicating that motor neuron degeneration was enhanced by the partial depletion of *Hsf-1* (Fig. 5m–p). Furthermore, haematoxylin and eosin staining demonstrated that skeletal muscle fibres were atrophied in the heterozygous *Hsf-1*-knockout AR-97Q mice compared with the genetically unmodified AR-97Q mice, suggesting the aggravation of neurogenic amyotrophy (Supplementary Fig. S6a,b).

Tissue-specific regulation of Hsps in SBMA mice. To confirm that the heterozygous knockout of *Hsf-1* leads to the downregulation of Hsps, we performed immunoblotting on several tissues from each mouse group. We found that the degree of Hsf-1 downregulation differed in a tissue-specific manner in the heterozygous *Hsf-1*-knockout SBMA mice. For example, the protein levels of Hsf-1 were significantly decreased by the heterozygous knockout of *Hsf-1* in the spinal cord, liver and skeletal muscle (Fig. 6a–d). Conversely, the expression levels of Hsf-1 were not changed in the testis of the heterozygous *Hsf-1*-knockout AR-97Q mice compared with the AR-97Q mice (Fig. 6a,e). In accordance with these findings, Hsp72, the inducible form of Hsp70, was downregulated in the spinal cord and liver, but not in the testis, of the heterozygous *Hsf-1*-knockout AR-97Q mice (Fig. 6a–c,e). Moreover, Hsp105 was also significantly downregulated in the spinal cord and liver of the heterozygous *Hsf-1*-knockout mice (Fig. 6a–c). However, the expression levels of Hsps within skeletal muscle were not changed by *Hsf-1* depletion (Fig. 6a,d). Similar findings were observed in the heterozygous *Hsf-1*-knockout wild-type mice compared with wild-type mice (Supplementary Fig. S7a–d). To confirm that the downregulation of Hsp72 following *Hsf-1* depletion was via the decrease of messenger RNA levels, we analysed the mRNA expression levels of *Hsp70A1*, the gene encoding Hsp72, in the spinal cord, liver and skeletal muscle. The results showed that the mRNA levels of *Hsp70A1* were decreased in the spinal cord and liver of the heterozygous *Hsf-1*-knockout AR-97Q mice, in agreement with the immunoblotting findings (Fig. 6f,g). In contrast, the heterozygous knockout of *Hsf-1* did not alter the mRNA levels of *Hsp70A1* in skeletal muscle (Fig. 6h). There were no detectable changes in the expression levels of Hsp40 and Hsp90 in all the tissues examined from heterozygous Hsf-1-knockout AR-97Q mice (Fig. 6a–e). These findings are compatible with the change in the distribution of pathogenic AR accumulation, and indicate that the induction of Hsp70 is dependent on the expression levels of Hsf-1 in the spinal cord and liver, but not in the skeletal muscle, of the SBMA model mice.

To elucidate the molecular machinery underlying the Hsf-1-independent regulation of Hsp70 expression in the skeletal muscle of AR-97Q mice, we investigated the expression levels of several major transcription factors, such as Nfya, Tbp, p53 and Sp1, which also regulate the expression of Hsp70 (refs 18,19, 35–37). The results showed that Nfya and Sp1, but not Tbp nor p53, were upregulated in the skeletal muscle of AR-97Q mice compared with wild-type mice (Fig. 7a). This upregulation was further enhanced by the partial depletion of *Hsf-1* (Fig.7a–c). In contrast to the skeletal muscle, neither Nfya nor Sp1 were upregulated by *Hsf-1* depletion in the spinal cord or liver of AR-97Q mice (Fig. 7d,e). Immunohistochemical analysis showed an increase in the levels of nuclear Nfya and Sp1 in the skeletal muscle of AR-97Q mice, which was further intensified by the heterozygous knockout of *Hsf-1* (Fig. 7f–h). These findings suggest that proteins such as Nfya and Sp1 appear to regulate the expression of Hsp70 and this probably underlies the observation that pathogenic AR accumulation was not increased in the skeletal muscle of the *Hsf-1*-depleted AR-97Q mice.

To investigate the effects of Hsf-1 on the pathogenic AR aggregations in the skeletal muscle, we analysed immunoblots of

the tissue using an anti-AR antibody. The results showed that the amount of oligomers or monomer of pathogenic AR was not increased by the heterozygous depletion of *Hsf-1* in the skeletal muscle of AR-97Q mice (Fig. 7i,j). In agreement with these immunoblot analyses, immunohistochemistry demonstrated no significant difference in the number of 1C2-positive cells

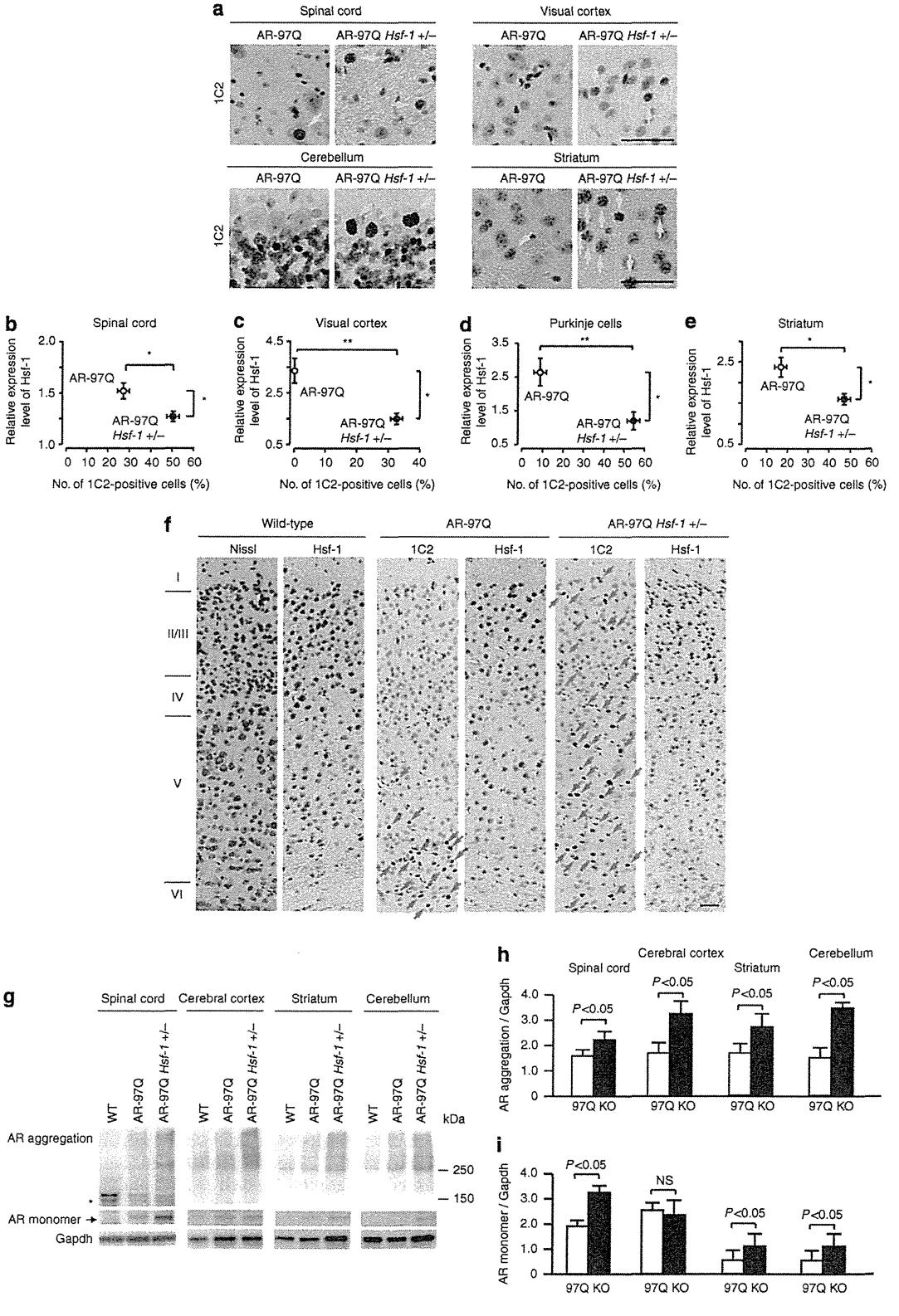

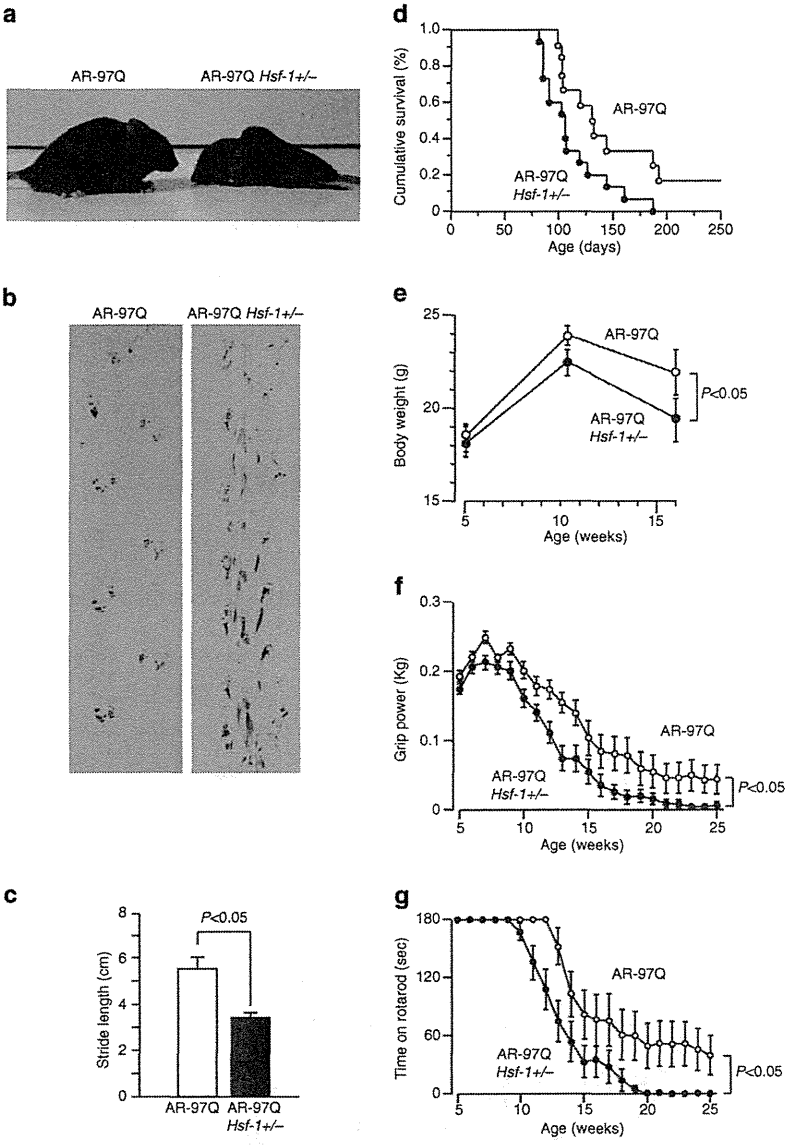

Figure 4 | Heterozygous *Hsf-1*-knockout AR-97Q mice have more severe muscle atrophy than AR-97Q mice. (**a**) Muscle atrophy is enhanced in the *Hsf-1*-knockout AR-97Q mice compared with the AR-97Q mice (10 weeks old). (**b**) Footprints of 13-week-old AR-97Q and *Hsf-1*-knockout AR-97Q mice. The front paws are shown in red, while the hind paws are shown in blue. (**c**) Quantification of the footprints revealed that the stride length was significantly shortened in the heterozygous *Hsf-1*-knockout AR-97Q mouse (13 weeks old). Unpaired *t*-test ($n=3$). Cumulative survival (**d**), body weight (**e**), grip power (**f**) and Rotarod task (**g**) of AR-97Q and *Hsf-1*-knockout AR-97Q mice. There were significant differences in all parameters between the AR-97Q ($n=12$) and heterozygous *Hsf-1*-knockout AR-97Q ($n=15$) mice by unpaired *t*-test: $P<0.05$ (**d**); $P<0.05$ at 16 weeks (**e**); $P<0.05$ at 25 weeks (**f**); and $P<0.05$ at 25 weeks (**g**). Error bars indicate s.e.m. (**c**–**g**).

Figure 3 | Augmentation of pathogenic AR accumulation in the CNS of *Hsf-1*-knockout AR-97Q mice. (**a**) Immunohistochemistry for 1C2, Hsf-1 and Hsp72 in AR-97Q and *Hsf-1*-knockout AR-97Q mice (13 weeks old). Pathogenic AR (yellow arrows) accumulated in the cerebral visual cortex of heterozygous *Hsf-1*-knockout SBMA mice where the accumulation of pathogenic AR was not observed in the AR-97Q mice. (**b**–**e**) The change in the relationship between the expression levels of Hsf-1 and the frequency of 1C2-positive neurons in the spinal anterior horn (**b**), cerebral visual cortex (**c**), Purkinje cells of the cerebellum (**d**) and striatum (**e**). (**f**) Immunohistochemistry for Hsf-1 and 1C2 in the cerebral motor cortex of AR-97Q and *Hsf-1*-knockout AR-97Q mice (13 weeks old). In AR-97Q mice, 1C2-positive cells were observed in the fifth layer of the cerebral motor cortex, where the expression levels of Hsf-1 were relatively lower than in the other layers. The distribution of pathogenic AR accumulation (red arrows) was expanded to the second and third layers of the cerebral motor cortex in heterozygous *Hsf-1*-knockout AR-97Q mice. (**g**) Immunoblotting for AR in wild-type, AR-97Q and *Hsf-1*-knockout AR-97Q mice (13 weeks old). Pathogenic AR oligomers are indicated by a smear from the top of the gel. *Nonspecific bands. (**h**) Quantitative analysis of immunoblots using densitometry indicated that the expression levels of abnormal AR protein complexes in the spinal cord, cerebral cortex, striatum and cerebellum were upregulated in heterozygous *Hsf-1*-knockout AR-97Q mice compared with AR-97Q mice. (**i**) Quantification of immunoblotting revealed that the expression levels of AR monomer were upregulated in the spinal cord, striatum and cerebellum of heterozygous *Hsf-1*-knockout AR-97Q mice. $^{*}P<0.05$, $^{**}P<0.01$ by unpaired *t*-test. More than 500 neurons from three brains were analysed in each group (**b**–**e**). Unpaired *t*-test ($n=3$) (**h**,**i**). Error bars indicate s.e.m. (**b**–**e**,**h**,**i**). Scale bars, 50 μm (**a**). NS, not significant.